Thermoelastic properties of microcracked polycrystals. Part II : The case of jointed polycrystalline TATB

Jean-Baptiste Gasnier, François Willot, Hervé Trumel, Dominique Jeulin, Maxime Biessy

Thermoelastic properties of microcracked polycrystals. Part II: The case of jointed polycrystalline TATB.

Jean-Baptiste Gasnier[a] François Willot[*a] Hervé Trumel[b] Dominique Jeulin[a] Maxime Biessy[b]

[a]Mines ParisTech, PSL Research University, Centre for Mathematical Morphology, 35 rue Saint-Honoré, F-77300 Fontainebleau, France. [b]CEA, DAM, Le Ripault, F-37260 Monts, France.
*Corresponding author (francois.willot@ensmp.fr).

Reference: ***International Journal of Solids and Structures*** **155, 2018, 257–274 (https://doi.org/10.1016/j.ijsolstr.2018.07.025). The text in the present document is the same as in the published article, page layout is different.**

Abstract The thermoelastic responses of a cracked TATB polycrystal is modeled using Fourier-based numerical computations and linear homogenization estimates. The numerical method is based on a Fourier scheme previously investigated (Gasnier et al., 2018) and the homogenization schemes include a new self-consistent estimate recently developed for cracked polycrystals. The effect of various populations of intergranular and transgranular microcracks are compared, with special attention to thermal behavior in the percolating regime. A model of micro-cracks is proposed for the TATB material in its initial state and the variations of the volumetric expansion coefficient of the TATB polycrystal under thermal cycles, during cooling and heating, are interpreted.

Keywords: Cracked polycrystals; Homogenization; Thermoelasticity; TATB

1 Introduction

Although obviously used for their detonation properties, explosives must also keep their integrity during their lifespan, when submitted to normal life loads (cyclic thermal loading, vibration, etc.) or to accidental ones (impacts, fire breakouts, etc.) Their thermomechanical behavior is therefore a crucial issue.

This is especially the case for a particular class of explosives, based on 1,3,5-triamino-2,4,6-trinitrobenzene (TATB), a powerful but highly stable explosive molecule that provides exceptional safety properties. As most explosives, TATB is an organic molecular crystal, with the $P\bar{1}$ triclinic symmetry (Cady and Larson, 1965), and comes as a yellow powder from synthesis. But as it decomposes before melting, it cannot be cast, and is instead manufactured by coating a TATB powder by a small amount of a polymer and isostatically pressing the coated powder at a pressure of several hundreds of MPa. The resulting slightly porous isotropic solid is therefore a TATB polycrystal jointed by the polymer that acts as a binder between TATB grains. This material is of the quasi-brittle kind, with a mechanical response somewhat comparable to that of concrete or rocks. It softens by microcracking, and under ordinary stress triaxiality, failure occurs at 1-2% longitudinal strain in uniaxial (stress) compression.

Besides, thermal expansion of TATB-based pressed explosives is an important engineering issue because, depending upon the thermal loading, it may be irreversible and result in dilatancy and an increase of porosity. This so called "ratchet growth" phenomenon has received considerable attention, because the safety characteristics of this class of energetic materials depend partly on porosity (see for example Dallman and Wackerle, 1993).

In their seminal work, Rizzo et al. (1981) performed a large number of cyclic thermal expansion experiments on pressed TATB-based materials with various binders, and even on binder-free pressed TATB. Their first and most important finding was that the thermal expansion of these various materials is indeed irreversible, although the TATB crystal undergoes purely reversible thermal expansion (Kolb and Rizzo, 1979; Sun et al., 2010), and that their volumetric thermal expansion coefficient is smaller than that of the TATB single crystal. The thermal expansion of the latter being strongly anisotropic, they concluded that this phenomenon should be attributed to the growth of internal stresses with temperature variations in the randomly oriented polycrystal, as is the case in polycrystalline graphite (Naum and Jun, 1970; Delannay et al., 2014), for instance.

The interpretation proposed by Rizzo et al. (1981) involving microstructural considerations, it appears straightforward to conduct microstructure-level simulations. Gee et al. (2007) and Maiti et al. (2008) performed mesoscale (i.e. grain scale) calculations using a molecular based computational tool. Accounting for the anisotropic thermoelastic behavior of the TATB single crystal, a grain-binder fracture model and a simplified, though three-dimensional, representation of the microstructure, they were able to reproduce the ratchet growth phenomenon qualitatively, and showed additionally that no dilatancy is predicted if the thermal expansion anisotropy of the TATB single crystal is not accounted for. Luscher et al. (2015) employed the standard self-consistent model to predict the thermal

expansion coefficients of (textured) TATB pressed uniaxially with no binder. These authors performed a purely thermoelastic parametric study of the effects of grain aspect ratio and porosity, and found that the self-consistent model allows predicting pronounced effective texture-induced thermal expansion anisotropy, and found that the porosity has a non negligible influence on this effect.

The present authors undertook recently (Ambos et al., 2015; Gasnier et al., 2015b) an effort to develop a microstructure-level Fourier-based homogenization framework applied to the above-described TATB-based material. A virtual microstructure model reproducing quantitatively the grain size and shape distributions or the real material was first developed, and used for FFT thermoelastic homogenization using published data for TATB single crystal properties (Bedrov et al., 2009; Kolb and Rizzo, 1979; Sun et al., 2010). The calculations were shown to overestimate the overall elastic properties by a large amount with respect to experimental measurements.

As shown below (see Section 2.1), this discrepancy is likely to be due to the presence of a pre-existing population of microcracks in the pristine material. Besides, it is shown in Section 2.2 that high and low temperature thermal cycles probably induce microcracking of different natures. The effect of populations of microcracks must therefore be investigated, in order to make progress in the understanding of the material in its pristine state and of the nature of microcracks induced by thermal cycling. This is the purpose of the present paper within the same FFT framework, but in the restricted context of general isotropy, owing on the one hand to the isotropic manufacturing process of the considered material, and on the other hand to the non directional character of thermal loading, provided that the experiments be performed sufficiently slowly to neglect thermal gradients in the samples.

The FFT method not being well adapted to accounting for zero-volume objects such as cracks, the expected computational biases have been thoroughly studied (see the companion paper Gasnier et al., 2018). It is shown how some strong biases can be avoided, especially regarding the orientation of a crack with respect to the voxel grid, and how the effect of the finite volume of cracks can be corrected, thus providing a low resource demanding and mesh-free full-field homogenization method to study the influence of microcracking on the thermoelastic effective properties of the material at stake.

This article is organized as follows. Section 2 gives a brief insight into the response of the material under uniaxial, triaxial and hydrostatic cyclic compression, and a detailed account of its response under high and low temperature cyclic thermal loading. Section 3 describes the virtual microstructures, TATB single crystal behavior, and the homogenization framework. Sections 5 and 6 give computational results for randomly oriented microcracks and for the case of correlated microcrack and crystallographic orientations. Sections 7 and 8 discuss the results and conclude the paper, respectively.

2 Experimental

The material has been described in detail previously (Ambos et al., 2015; Gasnier et al., 2015b). In brief, it consists in a TATB polycrystal jointed by around 5% (vol.) of an amorphous binder, glassy at ordinary temperature, and containing a few percent residual porosity. The average grain size (i.e. equivalent diameter) is around 40 µm, the largest ones being close to 100 µm. One of the most striking features is the pronounced non convexity of most TATB grains. In its initial state, this material contains a few intra- and transgranular microcracks. However, high magnification cannot be achieved with scanning electron microscopy because it tends to decompose if the energy density of the electron beam is too high. Therefore, we have not been able to distinguish eventual intergranular microcracks from grain boundaries by optical or scanning electron microscopy.

2.1 Mechanical response

This material has been thoroughly characterized under uniaxial compression and tension, at various temperatures and strain rates, and under triaxial and hydrostatic compression at various confining pressures. For illustration purposes, Fig. 1 compares the mechanical response of the material under uniaxial cyclic compression (black curve) and triaxial cyclic compression at 200 MPa confining pressure (grey curve). For legibility, the strain range $[-0.02; 0.01]$ has been enlarged in the inset. Strains are positive in tension. From the uniaxial compression curve, Young's and transverse moduli can be measured in the narrow linear zone, yielding bulk and shear moduli of 7.2 and 2.7 GPa respectively.

Fig. 2a illustrates the result of hydrostatic cyclic compression. Pressure is increased at 1 MPa.s^{-1}, up to 100 MPa, then decreased to zero at the same rate. After an uncontrolled time lag of a few minutes, the pressure is increased again to 200 MPa, and seven cycles are performed to maximum pressures of 100, 200, 300, 400, 600, 800 and 950 MPa.

As illustrated by Fig. 2a (the cycles at 800 and 950 MPa maximum pressure being omitted for legibility), the pressure-volumetric strain cycles are not reversible, and the material compacts progressively as pressure increases.

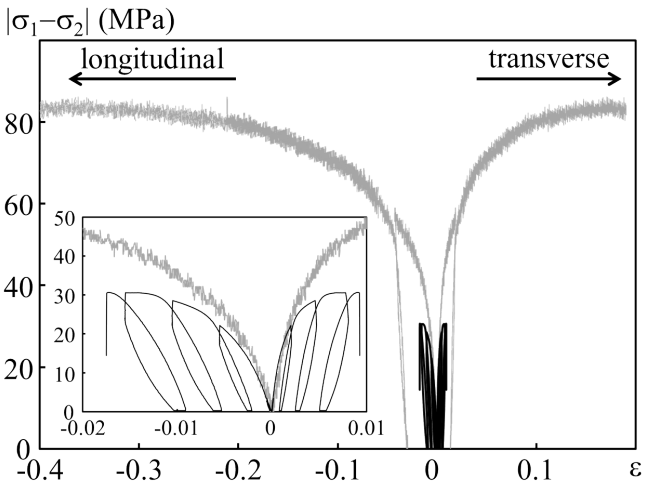

Figure 1: Principal stress difference $|\sigma_1 - \sigma_2|$ versus logarithmic longitudinal or transverse strain ϵ for uniaxial cyclic compression (in black) and triaxial compression (in grey). Negative strains are recorded by the longitudinal gauges, positive ones by the transverse gauges. The inset is a magnification of the $[-0.02; 0.01]$ strain range.

The maximum compaction represents less than half the total porosity, and is reached at 600 MPa, the 800 and 950 MPa cycles being almost reversible. For each cycle, as indicated in Fig. 2a, the initial slopes of loading and unloading are evaluated. The first one represents the effect of compaction (i.e. porosity reduction) on the zero-pressure bulk modulus, while the second one adds the effect of pressure, i.e. nonlinear elasticity, assuming reversible unloading.

The results are shown in Fig. 2b. Within the accuracy of the experiment, the zero-pressure bulk modulus is not influenced significantly by the compaction process. The high-pressure bulk modulus, on the other hand, increases rapidly between 100 and 600 MPa, then reaches a linear asymptote. The latter is interpreted as the effect of nonlinear elasticity, since no measurable compaction occurs above 600 MPa. The asymptote has the following linear form implying the well-known Murnaghan pressure-volume relationship (Murnaghan, 1951):

$$K(P) \equiv \frac{\partial P}{\partial \varepsilon_{kk}} = K_0 + kP, \tag{1}$$

with $K_0 = 14.5$ GPa and $k = 5$. This approximation holds to a very good approximation between 950 and 600 MPa, but not for lower pressures, for which the bulk modulus decreases much more rapidly. This is interpreted as the consequence of the presence of internal surfaces, i.e. microcracks, open at low pressure and closed at high pressure.

2.2 Thermal expansion response

2.2.1 The high temperature case

A thermal expansion experiment (Ambos et al., 2015) was first performed on an Adamel-Lhomargy DI-21 horizontal dilatometer above room temperature (Fig. 3a). A 5 × 5 × 50 mm sample was submitted to two heating-cooling cycles to 140°C at ±10 °C per hour to guarantee minimum temperature gradients. The maximum temperature (140 °C) was chosen to be above the glass temperature of the binder (∼100 °C).

The thermogram of Fig. 3a, in which heating phases are plotted in grey and cooling ones in black for legibility, displays several linear zones, referenced 1–8. Their corresponding slopes are gathered in Table 1.

During the first heating phase, linearity is lost early, at ∼45°C. Once the glass transition exceeded, thermal expansion increases dramatically. The irreversible character of the process in this zone is demonstrated by the non correspondence between heating and cooling phases. The two cooling phases being strictly parallel, they can reasonably be assumed as reversible. Moreover, the slopes of zones 4, 5 and 8 are very close, suggesting that phase 5 is also reversible. It can be concluded that most of the irreversible thermal expansion (or "ratchet growth") takes place above the glass transition temperature, although a small part occurs below (see Section 2.2.3). In the linear zones labeled 2 and 6, the irreversible dilatancy phenomenon occurs. Therefore, the corresponding slopes are not thermodynamic (i.e. reversible) thermal expansion coefficients, but only indicate phases of constant rate dilatancy.

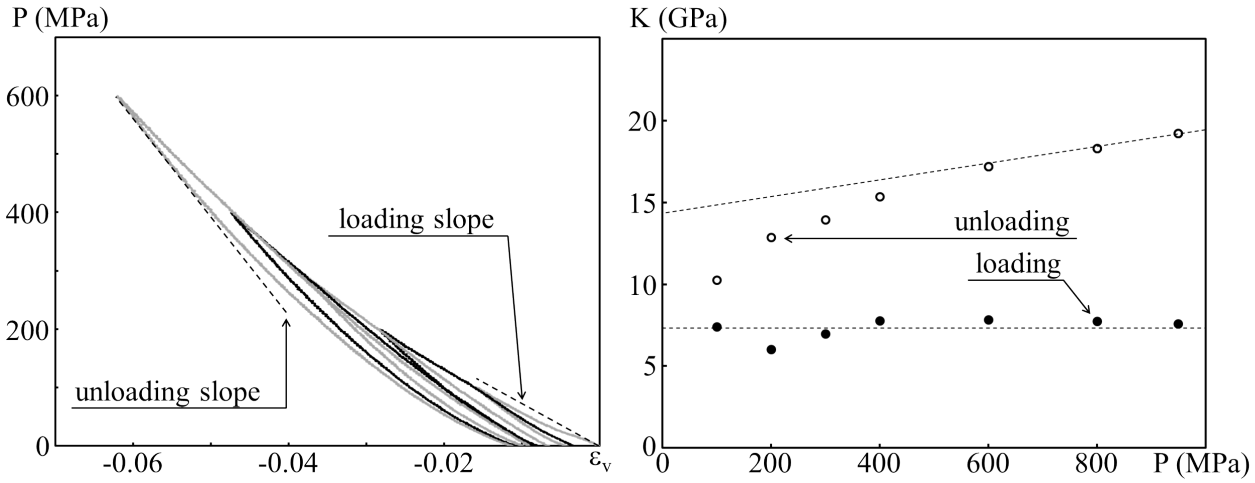

Figure 2: (a) Pressure P vs volumetric strain ϵ_v recorded in hydrostatic cyclic compression. For legibility, the cycles at 800 and 950 MPa maximum pressure are omitted. (b) Loading and unloading slopes K versus pressure P defined in (a) vs the maximum pressure of the corresponding cycle.

In the sequel, the denomination of "expansion coefficient" will be used as an abbreviation for thermodynamic volumetric thermal expansion coefficient.

The expansion coefficient of the beginning of the first heating phase (labeled 1 in Table 1) corresponds to that of the initial material in its glassy regime, and has a value of 1.442×10^{-4} K^{-1}. The expansion coefficient of the material in the glassy regime but after ratchet growth (linear phases labeled 4, 5 and 8 respectively) takes an average value of 1.827×10^{-4} K^{-1}, representing a $\sim 25\%$ increase. Above the glass transition temperature (linear zones labeled 3 and 7), the average (thermodynamic) expansion coefficient is 3.461×10^{-4} K^{-1}, which is almost twice the glassy value.

During the first heating-cooling cycle, a dilatancy (measured at 50°C) of 0.58% occurs, while the total dilatancy after the second thermal cycle is 0.73%. This is consistent with the well documented fact that dilatancy reaches a temperature-dependent asymptotic value for constant maximum temperature thermal cycling. Note that this also suggests that dilatancy is a time dependent process. This was verified by performing an experiment at a higher heating rate (not shown).

Table 1: Thermal expansion coefficients (in 10^{-4} K^{-1}) corresponding to the linear zones of the thermogram of Fig. 3a.

linear zone	slope	phase	linear zone	slope	phase
1	1.442	1st heating	5	1.794	2nd heating
2	4.644	1st heating	6	3.972	2nd heating
3	3.490	1st cooling	7	3.432	2nd cooling
4	1.835	1st cooling	8	1.851	2nd cooling

2.2.2 The low temperature case

A second experiment was performed at low temperature (see Fig. 4), with the $5 \times 5 \times 50$ mm geometry, and the same rate of ± 10 °C per hour (Gasnier et al., 2015b). The sample was submitted to four cooling-heating cycles from 40°C down to 0, −25, −50 and −75°C.

The cooling phase of the first cycle is almost linear, referenced 1 in Fig. 4a, with a corresponding expansion coefficient of 1.434×10^{-4} K^{-1}, down to ~ 5 °C. Below this temperature threshold, irreversible evolutions are observed. The beginning of re-heating is linear, illustrated by the dashed line referenced 3, associated to a lower expansion coefficient. The slope of the heating phases then increases up to the initial slope (dashed line referenced 2). Although the initial slope is recovered, a small dilatancy is recorded at the end of each cycle. To fix ideas,

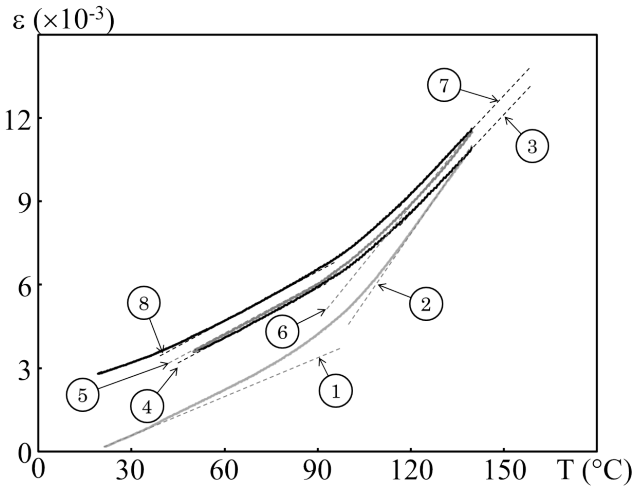

Figure 3: Thermal longitudinal strain ϵ versus temperature T for cyclic thermal loading above room temperature. The dashed lines correspond to linear zones of the thermogram, referred to through numbers (see text). Grey lines: heating; Black lines: cooling.

at the end of the last cycle, the dilatancy is only 8.7×10^{-4} (i.e. less than 0.1% volumetric strain). Finally, the beginning of the cooling phase of each cycle coincides very well with the heating phase of the previous cycle, except for the last cycle, for which a slight difference is noticed.

Table 2 gathers the expansion coefficients measured in the linear zone of the re-heating phase of each cycle, and compares them to those measured in the linear zone of the beginning of each re-cooling phase. As illustrated in Fig. 4b, the expansion coefficient of the beginning of re-heating phases decreases monotonically, whereas that of the beginning of the cooling phases remains constant to a good approximation.

Table 2: Volumic thermal expansion coefficients (in 10^{-4} K^{-1}) corresponding to the linear zones of the re-heating and cooling zones of the thermogram of Fig. 4.

cycle	heating slope	cooling slope
1	1.389	1.434
2	1.233	1.443
3	1.113	1.447
4	1.020	1.418

2.2.3 The sub-glass transition case

A complementary experiment was performed with a more recent and accurate dilatometer (dual sample Netzsch DIL 402 SE), to investigate the nonlinearity observed below the glass transition temperature. The sample geometry was identical as above, as was the loading rate. The sample was submitted to heating-cooling cycles from ambient temperature to maximum temperatures of 40, 60, 70, 80 and 90 °C, just below the glass transition temperature, and to a final cooling–heating cycle to −30 °C.

Fig. 5 shows the resulting global thermogram. A few limited artifacts are observed as undulations on the thermogram, and are due to a liquid nitrogen shortage perturbing the thermal control. The first three cycles are reversible, superimposed and virtually indistinguishable. A slight nonlinearity is noticed, compatible with a linear dependence of the expansion coefficient on temperature.

Between 70 °C and the glass transition, a slight irreversibility is observed. This finding is comparable to those observed in Fig. 3a, except that no variation in the expansion coefficients is noticed. Their average value is 1.476×10^{-4} K^{-1}, in the range [20; 50°C] with a maximum deviation of $8{\times}10^{-6}$ K^{-1}, and heating and cooling curves are strictly parallel in the same range. Also notice that the unloading phase of the cycle at 80 °C is very close to the heating phase of the following cyle, up to 80 °C, enforcing once again the reversibility of cooling.

The dilatancies are 2.5×10^{-4} for the cycle at 80 °C, and 5.6×10^{-4} for the cycle at 90 °C. These values, lower than 0.1% volumetric strain, are to be compared to those recorded at 140 °C (see Fig. 3a), namely 7.3×10^{-3}.

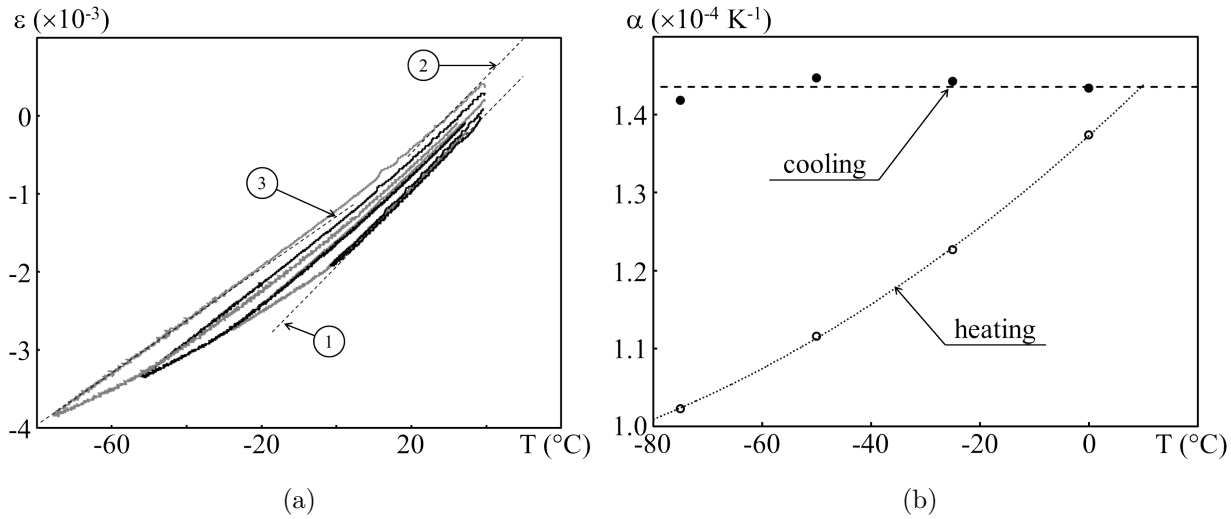

Figure 4: (a) Thermal longitudinal strain ϵ versus temperature T under cyclic thermal loading at low temperature. The dashed lines correspond to linear zones of the thermogram, referred to through numbers (see text). Black lines: first and third cycles; grey lines: second and fourth cycles. (b) Volumetric thermal expansion coefficients α measured in the linear phases of each cycle of the thermal experiment of Fig. 4a versus minimum temperature of each cycle. Filled symbols and dashed line: cooling; open symbols and dotted line: heating.

Finally, the last cycle at -30 °C exhibits a similar phenomenology as in Fig. 4a, namely a loss of linearity and a decrease of the expansion coefficient, measured here at 1.237×10^{-4} K^{-1}. The loss of linearity was observed at ~ 5 °C in the former case, ~ 25 °C in the present case.

2.2.4 Discussion

The above-described experimental results provide a wealth of information. First of all, the results illustrated in Figs. 3a, 4a and 5 provide close values of 1.442×10^{-4} K^{-1}, 1.434×10^{-4} K^{-1} and 1.476×10^{-4} K^{-1} respectively for the expansion coefficient of the material in its initial state. These values are significantly lower than that of the TATB single crystal (1.875×10^{-4} K^{-1}, see Section 3.2 for details), consistently with the observations of Rizzo et al. (1981).

The thermal experiments show that the reversibility domain is limited to [5; 70 °C] approximately, at least at ± 10 °C per hour. The behavior is slightly nonlinear, which could be due to the nonlinear thermal expansion of the TATB crystal, to that of the binder, or to both. Outside this domain, the thermal behavior is irreversible and strongly nonlinear but in a quite different fashion for high or low temperature loadings.

In the high temperature range, two cases should be distinguished. Between ~ 70 °C and the glass transition, dilatancy (hence ratchet growth) occurs, but has no measurable effect on the expansion coefficient. The dilatancies measured in this range are lower than 10^{-3}. Exceeding the glass transition induces approximately a doubling of the (thermodynamic) expansion coefficient. After thermal cycling, strong dilatancy and a $\sim 25\%$ increase of the glassy expansion coefficient are observed.

In the low temperature case, the main feature is the marked decrease of the expansion coefficient, followed by its rapid increase upon re-heating when approaching room temperature. A parallel can be drawn between this behavior and the mechanical response of quasi-brittle materials (see Fig. 6), which display tensile stiffness softening and stiffness recovery, attributed to the unilateral behavior of microcracks, upon reverse loading. Of course, the parallel is not complete, since mechanically-induced microcracking in quasi-brittle materials is highly directional while, due to the manufacturing process and thermal loading, the present material remains macroscopically isotropic throughout the thermal loading process.

Nevertheless, it may be used in a heuristic fashion to suggest that cooling at sufficiently low temperatures induces microcracking, whose opening provokes a decrease of the expansion coefficient and whose progressive closure occurs with the thermal load removal, thus explaining the initial expansion coefficient recovery. The small residual dilatancy observed after thermal cycling can likewise be interpreted as the effect of slightly incomplete microcrack closure.

Within the material, individual grains are supposedly randomly oriented. Since the latter displays strongly

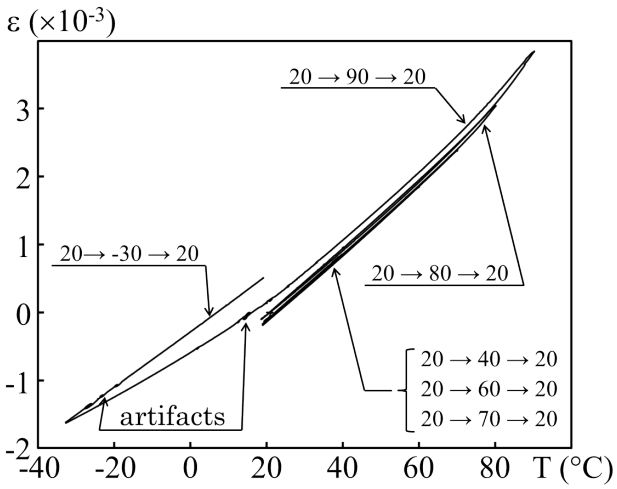

Figure 5: Thermal longitudinal strain ϵ versus temperature T under cyclic thermal loading between ambient and the glass transition temperature. The first three cycles (up to 70°C) are superimposed, reversible, and virtually indistinguishable.

anisotropic thermal expansion, the material response upon thermal loading should depend strongly on the binder properties and on the grain-binder bond strength.

In the low temperature case, the glassy binder is hard, and assuming high strength grain-binder bonds, the scenario put forward by Rizzo et al. (1981) suggests that internal stresses should build up and hinder partially the thermal expansion of individual grains, thus resulting in a macroscopic expansion coefficient lower than that of the single crystal. The binder then acts as a stress transmitter between grains. As the thermal load increases, so do internal stresses, and local fracture may eventually occur, be it debonding or grain fracture. In its glassy state, the binder remains very hard and is not likely to deform substantially, although plastic yielding cannot be ruled out. Hence, the material should behave essentially in an elastic fashion, thus explaining the very low level of dilatancy after the thermal load removal.

In the high temperature case, conversely, the binder softens and melts at the glass transition, then deforms massively, possibly cavitating, or debonds from the grains, to accommodate the displacement jumps at grains boundaries induced by the free anisotropic thermal expansion of grains, no longer hindered by internal stresses. Upon cooling, the binder hardens back at the glass transition, and freezes the material, including the newly created porosity. It should be remarked that in this case, the glass transition temperature becomes the new stress free state, from which internal stresses begin again to build up upon cooling.

In any case, internal stresses build up whether by cooling or by heating, both inducing damage. At this stage, whether microcracking is inter- or transgranular remains an open question, to be investigated in the following via microstructure level simulations. But considering the difference in response at high and low temperature, it seems likely that different mechanisms be involved.

3 Methodology and input data

3.1 Methodology

As stated in Section 1, previous FFT calculations (Ambos et al., 2015; Gasnier et al., 2015b) performed on the assumedly perfectly bonded TATB polycrystal yielded a strong overestimation of the bulk and shear overall moduli. The above described experimental results and the following discussion suggest (i) that the pristine material contains open microcracks, (ii) that thermal cycling induces microcracking, and (iii) that high and low temperature might produce microcracks of different kinds. Besides (see Gasnier et al., 2015b), the predicted overall volumetric thermal expansion coefficient coincides with the experimentally measured one of the pristine material if the thermal data of Sun et al. (2010) are used, but is strongly overestimated with those of Kolb and Rizzo (1979).

The objective of the present work is therefore to investigate all these different issues with a single tool, namely FFT-based homogenization on microstructures parametrized by the density of the populations of microcracks that they contain. Since the nature of the latter remains unknown, calculations will be performed on microstructures

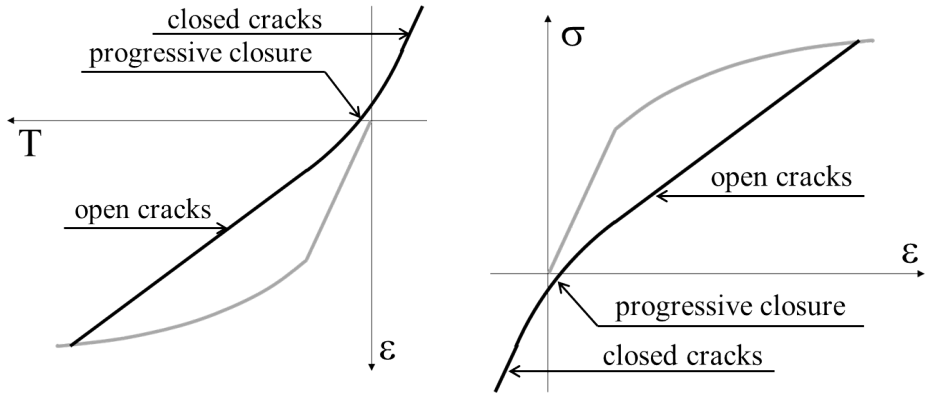

Figure 6: Parallel between (a) the thermal strain vs temperature low temperature cyclic response of the present material and (b) the stress-strain response of an idealized quasi-brittle material under tension and reverse compression. Cooling and loading in grey, re-heating and unloading in black.

containing either intergranular or transgranular microcracks. The case of intragranular ones is not considered here, for the sake of computational cost. As only the overall thermoelastic properties are sought, the investigation is performed in the context of linear (anisotropic) thermoelasticity for TATB. The presence of binder and porosity are disregarded, as an exploratory work showed that, within a purely thermoelastic context, their account yields only minor changes in the overall moduli (Gasnier et al., 2018). Finally, only the thermal data of Sun et al. (2010) will be used, this being justified *a posteriori* in Section 7.

3.2 TATB single crystal thermoelasticity

The linear thermoelastic law addressed in the present work takes the classical form:

$$\boldsymbol{\sigma}(\boldsymbol{x}) = \mathbf{C}(\boldsymbol{x}) : [\boldsymbol{\varepsilon}(\boldsymbol{x}) - \boldsymbol{\alpha}(\boldsymbol{x})\Delta T(\boldsymbol{x})] \,. \tag{2}$$

where $\boldsymbol{\sigma}(\boldsymbol{x})$ and $\boldsymbol{\varepsilon}(\boldsymbol{x})$ are the stress and strain fields respectively, and $\Delta T(\boldsymbol{x})$ is the local temperature increase, whereas $\mathbf{C}(\boldsymbol{x})$ and $\boldsymbol{\alpha}(\boldsymbol{x})$ are the elastic stiffness and thermal expansion tensors evaluated at point $\boldsymbol{x}$, but piecewise constant.

The TATB crystal is triclinic (system $P\bar{1}$ with two molecules per cell), and has cell parameters $a = 9.01$ Å, $b = 9.028$ Å and $c = 6.812$ Å, and cell angles $\alpha = 108.59°$, $\beta = 91.82°$ and $\gamma = 119.97°$ (Cady and Larson, 1965). The TATB molecules being essentially planar, they establish hydrogen bonds between adjacent nitro- (NO_2) and amino- (NH_2) groups and assemble in graphitic planes, themselves only weakly bonded by van der Waals interactions.

The elastic moduli used in the present work for the TATB crystal are those obtained by Bedrov et al. (2009) via molecular dynamics computations:

$$\mathbf{C}^{\mathrm{T}} = \begin{pmatrix} 65.7 & 18.5 & 4.0 & -0.2 & -1.0 & 1.0 \\ & 62.0 & 5.0 & 0.6 & -0.5 & 1.0 \\ & & 18.3 & 0.2 & -0.4 & -0.4 \\ & & & 1.4 & 0.1 & 0.3 \\ & \mathrm{sym} & & & 0.68 & 0.4 \\ & & & & & 21.6 \end{pmatrix} \quad [\mathrm{GPa}], \tag{3}$$

where $\mathbf{C}^{\mathrm{T}}$ is expressed in the system $(\mathrm{e}_1, \mathrm{e}_2, \mathrm{e}_3)$ for which e_1 is aligned with the cell parameter a, e_2 lies in the (a, b) plane, and $\mathrm{e}_3 = \mathrm{e}_1 \wedge \mathrm{e}_2$. Eq. (3) uses the Voigt notation:

$$(\sigma_{11}, \sigma_{22}, \sigma_{33}, \sigma_{23}, \sigma_{13}, \sigma_{12})^{\mathrm{t}} = \mathbf{C}^{\mathrm{T}} \cdot \left[(\varepsilon_{11}, \varepsilon_{22}, \varepsilon_{33}, 2\varepsilon_{23}, 2\varepsilon_{13}, 2\varepsilon_{12})^{\mathrm{t}} - (\alpha^{\mathrm{T}}_{11}, \alpha^{\mathrm{T}}_{22}, \alpha^{\mathrm{T}}_{33}, 2\alpha^{\mathrm{T}}_{23}, 2\alpha^{\mathrm{T}}_{13}, 2\alpha^{\mathrm{T}}_{12})^{\mathrm{t}} \Delta T\right] . \tag{4}$$

Some level of crystal symmetries is most often required to apply analytical homogenization methods. When

needed, the following hexagonal approximation of (3) will be used:

$$\mathbf{C}^{\mathrm{T}} \approx \mathbf{C}^{\mathrm{H}} = \begin{pmatrix} 63.9 & 18.5 & 4.5 & 0 & 0 & 0 \\ & 63.9 & 4.5 & 0 & 0 & 0 \\ & & 18.3 & 0 & 0 & 0 \\ & & & 1.04 & 0 & 0 \\ & \mathrm{sym} & & & 1.04 & 0 \\ & & & & & 22.7 \end{pmatrix} \quad [\mathrm{GPa}], \tag{5}$$

The form above amounts to the "Euclidean projection" as given by Moakher and Norris (2006), except for the moduli 11, 22, 12 and 66. The latter have been computed by keeping $C^{\mathrm{T}}_{12} = C^{\mathrm{H}}_{12}$ and enforcing the same response to hydrostatic strain loading, i.e. the mean of the elastic moduli of $\mathbf{C}^{\mathrm{T}}$ and $\mathbf{C}^{\mathrm{H}}$ in the top-left quadrant are equal. The Euclidean projection provides the slightly different moduli $C_{12} = 19.0$ and $C_{11} = 63.3$.

The thermal expansion coefficients used in the present work for TATB are derived from the X-ray diffraction measurements of Sun et al. (2010):

$$\boldsymbol{\alpha}^{\mathrm{T}} = \begin{pmatrix} 12.29 & -0.95 & 19.41 \\ & 9.022 & -37.39 \\ \mathrm{sym} & & 166.2 \end{pmatrix} \times 10^{-6}\mathrm{K}^{-1}. \tag{6}$$

Earlier X-ray diffraction measurements of Kolb and Rizzo (1979) yield sensibly different values, and will not be considered herein. Again, the following transverse-isotropic approximation will be used when needed:

$$\boldsymbol{\alpha}^{\mathrm{T}} \approx \boldsymbol{\alpha}^{\mathrm{H}} = \begin{pmatrix} 10.66 & 0 & 0 \\ & 10.66 & 0 \\ \mathrm{sym} & & 166.2 \end{pmatrix} \times 10^{-6}\mathrm{K}^{-1}. \tag{7}$$

No eigen value has been computed in the above approximation. Instead, we simply kept α^{T}_{33}, averaged α^{T}_{11} and α^{T}_{22} and replaced other coefficients by 0. This simple approach has been followed to ensure that tensors $\mathbf{C}^{\mathrm{H}}$ and $\boldsymbol{\alpha}^{\mathrm{H}}$ have the same axis of symmetry in the hexagonal approximation, a condition for applying most analytical homogenization schemes.

Eqs. (3) and (6) show very strong anisotropy of the single crystal thermoelastic behavior, illustrated by a ratio of more than 15 between C^{T}_{66} and the other two shear moduli, and between α^{T}_{33} and the other two principal thermal expansion coefficients. Note also that the elastic moduli in (3) are close to that of a tensor of hexagonal symmetry with stiff "transverse" Young modulus along directions 1 and 2, and soft normal Young modulus along direction 3. This is also true for thermal expansion, although the component α^{T}_{23} cannot be totally neglected.

The data of Sun et al. (2010) display a moderate nonlinearity in the thermal expansion of the crystal cell parameter c. Its thermal expansion coefficient $(1/c)\partial c/\partial T$ is 1.493×10^{-4} K^{-1} at 20 °C, and 1.692×10^{-4} K^{-1} at 140 °C, representing a 13% increase. This nonlinearity could at least partly explain that observed in the macroscopic thermal expansion experiments of Section 2.2.3.

3.3 Homogenization

Rotation tensors are used to determine the local elastic moduli and thermal dilation components in each grain. More precisely, we set:

$$C_{ij,kl}(\boldsymbol{x}) = R_{iI}(\boldsymbol{x})R_{jJ}(\boldsymbol{x})R_{kK}(\boldsymbol{x})R_{lL}(\boldsymbol{x})C^{\mathrm{T}}_{IJ,KL}, \quad \alpha_{ij}(\boldsymbol{x}) = R_{iI}(\boldsymbol{x})R_{jJ}(\boldsymbol{x})\alpha^{\mathrm{T}}_{IJ}, \tag{8}$$

where $\mathbf{C}^{\mathrm{T}}$ and $\boldsymbol{\alpha}^{\mathrm{T}}$ are the stiffness and thermal expansion tensors (3) and (6), which are expressed in the coordinates system of the laboratory, and $\mathbf{R}$ is a constant-per-grain rotation tensor. Its rotation angle is uniformly-distributed in the interval $[0;\pi]$ and its axis is oriented uniformly on the sphere. Furthermore, the rotation tensors of different grains are uncorrelated:

$$E\left[\mathbf{R}(\boldsymbol{x}) \otimes \mathbf{R}(\mathbf{y})\right] = E\left[\mathbf{R}(\boldsymbol{x})\right] \otimes E\left[\mathbf{R}(\mathbf{y})\right], \quad \mathbf{x} \text{ and } \mathbf{y} \text{ lie in different grains.} \tag{9}$$

where $E[\cdot]$ designates expected values. This simplifying assumption is used to alleviate the lack of experimental data on the field $\mathbf{R}(\mathbf{x})$. The polycrystaline material has been pressed from an initial powder in a process that likely involves plastic deformation. Thus, a correlation presumably exists between the crystal directions and geometrical features of the grains such as elongation, in contrast with (9). This effect is neglected in the present study.

The macroscopic loading is specified by periodic boundary conditions prescribed on a computational domain Ω containing $L \times L \times L$ voxels, and by an average strain $\overline{\boldsymbol{\varepsilon}}$ and thermal loading $\overline{\Delta T}$:

$$\boldsymbol{\varepsilon}\#, \qquad \boldsymbol{\sigma}\cdot\mathbf{n} - \#, \qquad \langle\boldsymbol{\varepsilon}(\boldsymbol{x})\rangle = \overline{\boldsymbol{\varepsilon}}, \qquad \langle\Delta T(\boldsymbol{x})\rangle = \overline{\Delta T}, \tag{10}$$

where $\langle\cdot\rangle$ denotes a spatial average over Ω, $\#$ denotes periodicity with elementary cell Ω, $-\#$ anti-periodicity, and $\mathbf{n}$ is the normal along the boundary of Ω. In the rest of this work, we neglect thermal fluctuations and identify $\Delta T(\boldsymbol{x})$ with $\overline{\Delta T}$. Furthermore, small-strain and quasi-static equilibrium is assumed at any step during loading, i.e.:

$$\varepsilon_{ij}(\boldsymbol{x}) = (1/2)\left[\partial_i u_j(\boldsymbol{x}) + \partial_j u_i(\boldsymbol{x})\right], \qquad \partial_i \sigma_{ij}(\boldsymbol{x}) \equiv 0, \tag{11}$$

where $\mathbf{u}(\boldsymbol{x})$ is the (non-periodic) displacement vector field. The effective stiffness tensor $\widetilde{\mathbf{C}}$ and thermal expansion tensor $\widetilde{\boldsymbol{\alpha}}$ of the polycrystal relate the mean strain and stress response as:

$$\overline{\boldsymbol{\sigma}} = \widetilde{\mathbf{C}} : \left(\overline{\boldsymbol{\varepsilon}} - \widetilde{\boldsymbol{\alpha}}\overline{\Delta T}\right). \tag{12}$$

The effective properties are determined, in general, by applying six independent strain loadings ($\overline{\boldsymbol{\varepsilon}} \neq \mathbf{0}$, $\overline{\Delta T} = 0$) and one thermal loading ($\overline{\boldsymbol{\varepsilon}} = \mathbf{0}$, $\overline{\Delta T} \neq 0$). In the present study, all microstructure models are macroscopically isotropic and we restrict ourselves to the following hydrostatic and simple-shear strain loadings, and purely-thermal loading:

$$\overline{\varepsilon}_{ij} = \delta_{ij}, \qquad \overline{\Delta T} = 0, \tag{13a}$$

$$\overline{\varepsilon}_{ij} = \delta_{i1}\delta_{j2} + \delta_{i2}\delta_{j1}, \qquad \overline{\Delta T} = 0, \tag{13b}$$

$$\overline{\varepsilon}_{ij} = 0, \qquad \overline{\Delta T} = 1. \tag{13c}$$

The values of the overall strain loadings (100%) need not be realistic since linear behavior is assumed. The above conditions provide respectively the effective bulk and shear moduli $\widetilde{\kappa}$ and $\widetilde{\mu}$, and the effective volumetric expansion coefficient $\widetilde{\alpha}_V = \mathrm{tr}(\widetilde{\boldsymbol{\alpha}})$.

The equations for the local (2) and effective response (12) read, in terms of the compliance tensors $\mathbf{S}(\boldsymbol{x}) = \mathbf{C}^{-1}(\boldsymbol{x})$ and $\widetilde{\mathbf{S}} = \widetilde{\mathbf{C}}^{-1}$:

$$\boldsymbol{\varepsilon}(\boldsymbol{x}) = \mathbf{S}(\boldsymbol{x}) : \boldsymbol{\sigma}(\boldsymbol{x}) + \boldsymbol{\alpha}(\boldsymbol{x})\overline{\Delta T}, \qquad \overline{\boldsymbol{\varepsilon}} = \widetilde{\mathbf{S}} : \overline{\boldsymbol{\sigma}} + \widetilde{\boldsymbol{\alpha}}\overline{\Delta T}. \tag{14}$$

Compliance rather than stiffness tensors will be used whenever they provide simpler expressions. The compliance tensor of hexagonal crystals with axis of symmetry along e_3 has the following form:

$$\mathbf{S}^{\mathrm{H}} = \begin{pmatrix} 1/E_p & -\nu_p/E_p & -\nu_{pz}/E_p & 0 & 0 & 0 \\ & 1/E_p & -\nu_{pz}/E_p & 0 & 0 & 0 \\ & & 1/E_z & 0 & 0 & 0 \\ & & & 1/G_{zp} & 0 & 0 \\ & \mathrm{sym} & & & 1/G_{zp} & 0 \\ & & & & & 2\left(1+\nu_p\right)/E_p \end{pmatrix}, \tag{15}$$

where E_p is the Young modulus along directions e_1 and e_2, E_z along e_3, G_{zp} the shear modulus in planes parallel to e_3 and ν_p, ν_{pz} are Poisson coefficients. The form (15) refers to the following Voigt notation:

$$(\varepsilon_{11}, \varepsilon_{22}, \varepsilon_{33}, 2\varepsilon_{23}, 2\varepsilon_{13}, 2\varepsilon_{12})^{\mathrm{t}} = \mathbf{S}\cdot(\sigma_{11}, \sigma_{22}, \sigma_{33}, \sigma_{23}, \sigma_{13}, \sigma_{12})^{\mathrm{t}} + (\alpha_{11}, \alpha_{22}, \alpha_{33}, 2\alpha_{23}, 2\alpha_{13}, 2\alpha_{12})^{\mathrm{t}}\overline{\Delta T} \tag{16}$$

For the TATB crystal, the following values of $E_p = 57.9$ GPa, $E_z = 17.8$ GPa, $G_{zp} = 1.0$ GPa, $\nu_p = 0.28$, $\nu_{pz} = 0.18$ are computed from the approximate transversely isotropic elastic tensor given in Eq. (5). The contrast of properties in the in-plane and out-of-plane directions is about $E_p/E_z \approx 3.3$ in terms of Young moduli and $S_{44}/S_{66} \approx 47$ in terms of shear moduli.

3.4 Probabilistic microstructure models

Two types of polycrystal morphology are considered for the grains. Our main model is an "anisotropic Johnson–Mehl" tessellation, denoted (JM), which contains non-convex grains and is representative of the grains's granulometry and eccentricity distributions (Gasnier et al., 2015b,a). It is based on an underlying set of germs that follows a Poisson point process in time and space, as in the classical Johnson–Mehl model, but also uses an anisotropic "ellipsoidal" distance function attached to each germ that monitors the grains mean elongation. In addition, we

also consider the standard Voronoi tessellation, denoted (V). The Voronoi model (Stoyan et al., 1995; Ferenc and Néda, 2007) is based on a Poisson point process for the germs, and uses the Euclidean distance.

In the following, cracks are modeled by a set of thin, porous inclusions. In doing so, we assume that all cracks are open. In particular they offer no resistance to tangential slip. Inside cracks we set, accordingly, $\mathbf{C}(\boldsymbol{x}) = \mathbf{0}$, $\boldsymbol{\sigma}(\boldsymbol{x}) = \mathbf{0}$ and $\boldsymbol{\alpha}(\boldsymbol{x}) = \mathbf{0}$. Cracks have a small but strictly-positive width w. The latter takes on values ranging from 1 to 7 voxels.

Both intergranular and transgranular cracks are considered. Intergranular cracks, which occur along the interface separating two adjacent grains, are planar for the Voronoi model and non-planar for the Johnson–Mehl model. Transgranular cracks, defined by the intersection of a grain and a plane, are planar irrespective of the tessellation model, but may not be simply connected in the Johnson–Mehl tessellation. In the following, polycrystal models with intergranular cracks are denoted (JM-I) for the Johnson–Mehl tessellation and (V-I) for the Voronoi tessellation. Similarly, models with transgranular cracks are denoted (JM-T) and (V-T). Simulations of the (JM-I) and (JM-T) models are visible in Figs. 7a and b. In the four models, the presence of a crack at a point $\boldsymbol{x}$ in the domain, or the cracks's direction, is uncorrelated to the local crystal orientation at point $\boldsymbol{x}$.

The underlying probabilistic models for inter and transgranular cracks are as follows. Transgranular cracks are simulated using Poisson planes. These planes are generated by a point, which follows a homogeneous Poisson point process in Ω, and a random direction, taken uniformly on the sphere. A grain that intersects a given plane is then chosen randomly, resulting in a transgranular crack in that grain. Here again, the same probability is assigned to all grains intersected by the plane. The probabilty of intersection with a plane increases with the grain's size.

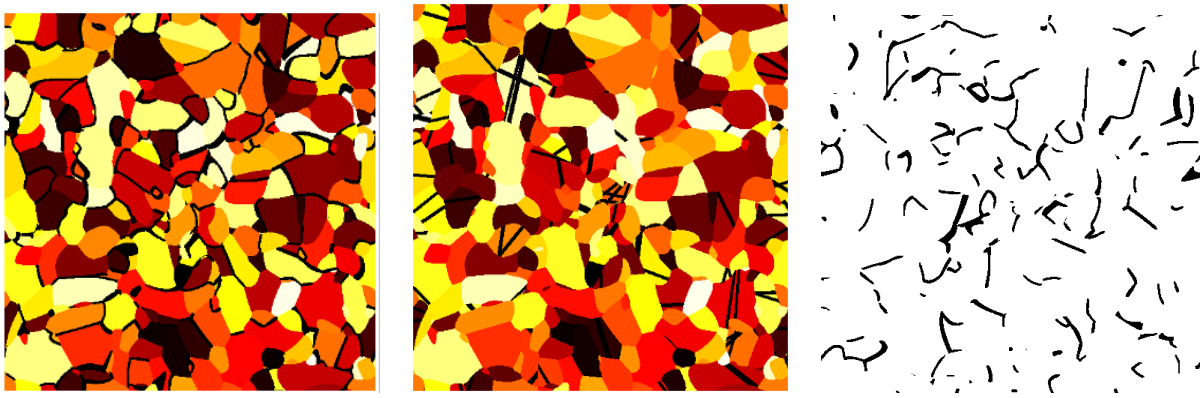

(a) (b) (c)

Figure 7: 2D sections of an anisotropic Johnson–Mehl tessellation with (a) intergranular and (b) transgranular cracks (black), denoted JMA-I and JMA-T respectively. Discretization: 512^3 voxels and $w = 4$ voxels. The cracks take 10% (JMA-I) and 4% (JMA-T) of all voxels. (c) 2D section of a binary Johnson–Mehl tessellation, obtained by replacing the grains in (a) by an homogeneous matrix.

To simulate intergranular cracks, we first determine all grain faces, identified by couples of adjacent grains. Cracks are implemented by selecting randomly a face. In this process, each face is assigned the same probability, so that cracks are as likely to occur along faces with high and low surface areas. In order to explore the effect of crystal anisotropy, we also introduce "binary" models of (JM-I) and (V-I) made of cracks embedded in an isotropic homogeneous matrix. These models amount to replace the grains by a homogeneous matrix while keeping all intergranular cracks intact (see Fig. 7c). Therefore the models do not contain any tessellation of space, but only a signature, through its cracks population. We denote them (JM-IB) for the Johnson–Mehl tessellation and (V-IB) for the Voronoi one. In the following, the elastic moduli of the matrix in the two models will be chosen equal to that of the uncracked polycrystal media, (JM) or (V) resulting in an isotropic macroscopic behavior.

To carry out full-field micromechanical computations, we discretize random realizations of the microstructure models on regularly-spaced grids containing L^3 voxels. First, we identify each voxel by its center $\boldsymbol{x}$ in the continuum space, and assign it a grain label G. Second, we discretize the cracks. Intergranular cracks $C_{\mathcal{I}}$ and transgranular cracks $C_{\mathcal{T}}$ are determined each as a set of voxel centers:

$$C_{\mathcal{I}} = \left\{\boldsymbol{x} : |\boldsymbol{x}-\boldsymbol{y}| \leq w/2,\, |\boldsymbol{x}-\boldsymbol{y}'| \leq w/2,\, \boldsymbol{y} \in \mathrm{G},\, \boldsymbol{y}' \in \mathrm{G}'\right\}, \tag{17a}$$

$$C_{\mathcal{T}} = \left\{\boldsymbol{x} \in G; \quad \mathrm{d}(\boldsymbol{x};\Pi) \leq w/2\right\}, \tag{17b}$$

where G, G' are grains, Π is a random Poisson plane and $\mathrm{d}(\boldsymbol{x};\Pi)$ is the distance from point $\boldsymbol{x}$ to Π.

The two models of cracks, intergranular and transgranular, each depend on one parameter. Populations of intergranular cracks are monitored by the probability that a crack is present along a grain face, and populations of transgranular cracks by the density of Poisson planes. These two parameters are not employed in this work. Instead we use the dimensionless cracks-density parameter η defined by Budiansky and O'Connell (1976):

$$\eta = \frac{2\mathcal{N}}{\pi} \left\langle A^2/P \right\rangle_{\mathcal{I},\mathcal{T}}, \tag{18}$$

where A and P are the surface area and perimeter of a crack, $\mathcal{N}$ is the mean number of cracks per unit volume and $\langle\cdot\rangle_{\mathcal{I},\mathcal{T}}$ denotes an average over all intergranular or transgranular cracks. To avoid the cumbersome computations that would be necessary to apply (18) to cracks $C_{\mathcal{I}}$ and $C_{\mathcal{T}}$, we use the following specialized formula, obtained for elliptical cracks of major axis a and minor axis b:

$$\eta = \frac{\pi\mathcal{N}}{2} \left\langle \frac{ab^2}{E\left(k\right)} \right\rangle_{\mathcal{I},\mathcal{T}} \qquad k = \sqrt{1 - b^2/a^2}, \tag{19}$$

where k the ellipse's eccentricity and $E(k) = \int_0^{\pi/2} \mathrm{d}\theta \sqrt{1 - k^2 \sin^2\theta}$ refers to the complete elliptic integral of the second kind. In practice, the semi-axis a and b entering (19) are evaluated using 3D inertia moments. Table 3 gives average values for the larger, middle and lower semi-axis, for two realizations of models (V-I) and (JM-I). As expected, the two largest semi-axis, used to compute η, are significantly higher than the third one. The length of the latter, smaller than $w/2$, shows that the cracks's thickness, resulting from the discretization, is different from w. This is because the number of voxels that are at a distance less than w from a given point is a step function. Obviously these discretization effects are most important for small values of w, typically in the range $[0.5; 5]$.

All numerical computations undertaken below are carried out using two random realizations of each model, on grids containing $M^3 = 512^3$ voxels. The number of grains is about 1400 in the Voronoi tessellation and about 2800 in the Johson-Mehl tessellation. We follow Ambos et al. (2015) and use the norm of the stress divergence vector as convergence criterion, with error criterion set to 10^{-4}.

Table 3: Mean values of the three semi-axis $c \leq b \leq a$ of the equivalent ellipsoids of cracks present in two realizations of models (V-I) and (JM-I). Values are given in voxels. The width of the cracks is $w = 4$ voxels and the cracks-density parameter is $\eta \approx 0.56$ (JM-I) and $\eta \approx 0.48$ (V-I).

Model	$\langle a\rangle_{\mathcal{I}}$	$\langle b\rangle_{\mathcal{I}}$	$\langle c\rangle_{\mathcal{I}}$
V-I	24.0	14.5	1.5
JM-I	18.5	9.3	1.5

The loss of connectivity of the solid phase is essential for understanding the mechanical properties of intergranular and transgranular models. This percolation threshold is given for model (V-I) as a proportion of about 8.2% of intact grain facets by Jerauld et al. (1984), i.e. 91.8% of cracked facets. To validate our model, we carry out numerical simulations of model (V-I) with increasing proportion of cracked facets equal to 90%, 92% and 94%. For simplicity, the realizations are obtained using the same Voronoi tessellation but independently choosen cracked facets. The number of percolating microstructures is found to be 1, 6 and 10 over 10 realizations for 90%, 92% and 94% of cracked facets, respectively, in agreement with Jerauld et al. (1984). For model (JM-I), we find a number of percolating configurations equal to 0, 6 and 10 over 10 microstructures, for a proportion of cracked facets equal to 92%, 94% and 96%, respectively. The crack density near the percolation threshold, computed when the proportion of cracked facets is 92% (V-I) and 94% (JM-I), gives the rough estimate $\eta \approx 0.46$ (V-I) and $\eta \approx 0.61$ (JM-I) at percolation. This suggests a higher percolation threshold for the intergranular Johnson–Mehl models (JM-I) and (JM-IB) compared to their Voronoi counterparts (V-I) and (V-IB), both in terms of the proportion of cracked grain facets and crack-density parameter.

No percolation threshold occurs for the transgranular crack models (JM-T) or (V-T), i.e. the solid phase is macroscopically connected when η is finite. In particular, percolating paths are guaranteed to exist in the vicinity of grain boundaries, where the crack tips are located.

4 Homogenized thermoelastic properties of cracked polycrystals

4.1 Self-consistent schemes and bounds

Many self-consistent schemes and bounds of interest to this study apply to either a cracked body that is otherwise homogeneous and isotropic, or to uncracked polycrystals. We combine the two types of methods to take into account

(a) (b) (c)

Figure 8: Schematic 2D view of the analytical estimates's underlying assumption. Cracks in black and grain boundaries in grey. (a): SC, NIA, HS. (b): SC′; (c): SC-TW.

both crystal anisotropy and cracks. For the elastic properties of uncracked polycrystals, we use Berryman's self-consistent scheme (Berryman, 2005). In the case of hexagonal symmetry of the crystal, the method consists in solving the system of three unknowns G, K, and ξ:

$$\begin{aligned} 3G_V &= C^{\mathrm{H}}_{33}+C^{\mathrm{H}}_{11}-2C^{\mathrm{H}}_{13}-C^{\mathrm{H}}_{66}, \qquad 6(K+2G)\xi = G(9K+8G), \\ 9K_V &= C^{\mathrm{H}}_{33}+2C^{\mathrm{H}}_{11}+2C^{\mathrm{H}}_{12}+4C^{\mathrm{H}}_{13}, \quad 3K_V\xi = 3(G_V+\xi)K - C^{\mathrm{H}}_{33}\left(C^{\mathrm{H}}_{11}+C^{\mathrm{H}}_{66}\right)+\left(C^{\mathrm{H}}_{13}\right)^2, \\ \frac{5}{G+\xi} &= \frac{K_V+\frac{4}{3}G}{\left(K+\frac{4}{3}G\right)(G_V+\xi)}+\frac{2}{C^{\mathrm{H}}_{44}+\xi}+\frac{2}{C^{\mathrm{H}}_{66}+\xi}, \end{aligned} \tag{20}$$

where G is the effective shear modulus, K the effective bulk modulus, ξ is an auxiliary variable and the C^{H}_{ij} refer to the hexagonal approximation to the TATB stiffness tensor (5). Although the TATB is better approached by a monoclinic symmetry, most methods developed for this class of polycrystals are bounds (Watt, 1980) rather than estimates, and are not considered hereafter. Also, the effective volumetric thermal expansion coefficient $\widetilde{\alpha}_V$ of a polycrystal with hexagonal symmetry is given exactly by the formula of Hashin (1984):

$$\widetilde{\alpha}_V = \widetilde{\alpha}_{11}+\widetilde{\alpha}_{22}+\widetilde{\alpha}_{33} = \alpha^{\mathrm{H}}_V + (\alpha^{\mathrm{H}}_{33}-\alpha^{\mathrm{H}}_{11})\frac{1/\widetilde{K}-S^{\mathrm{H}}_{iikk}}{S^{\mathrm{H}}_{ii33}-S^{\mathrm{H}}_{ii11}}, \tag{21}$$

where $\alpha^{\mathrm{H}}_V = \alpha^{\mathrm{H}}_{11}+\alpha^{\mathrm{H}}_{22}+\alpha^{\mathrm{H}}_{33}$, $\widetilde{K} = 1/\widetilde{S}_{iikk}$ is the polycrystal's effective bulk modulus, $\mathbf{S}^{\mathrm{H}} = \left(\mathbf{C}^{\mathrm{H}}\right)^{-1}$ the compliance tensor of the TATB, and $\boldsymbol{\alpha}^{\mathrm{H}}$ the hexagonal approximation (7) of the TATB dilation coefficients. For the uncracked TATB polycrystal, Eqs. (20) and (21) give $K = \widetilde{K} \approx 16.98$ GPa, $G \approx 6.85$ GPa and $\widetilde{\alpha}_V \approx 1.49\times10^{-4}\,\mathrm{K}^{-1}$.

Cracks are taken into account by several means. We first consider the self-consistent estimate of O'Connell and Budiansky (1974) and Budiansky and O'Connell (1976) which applies to a homogeneous isotropic body containing randomly-oriented cracks. Budiansky and O'Connell consider elliptical cracks with arbitrary aspect ratio but remark that their estimate is nearly insensitive to aspect ratio. Hereafter we use the formula obtained for disks, which is determined by the following:

$$\frac{K_{\mathrm{SC}}}{K} = 1-\frac{16}{9}\frac{1-\nu^2_{\mathrm{SC}}}{1-2\nu_{\mathrm{SC}}}\eta, \quad \eta = \frac{45}{16}\frac{(\nu-\nu_{\mathrm{SC}})(2-\nu_{\mathrm{SC}})}{(1-\nu^2_{\mathrm{SC}})\left[10\nu-\nu_{\mathrm{SC}}(1+3\nu)\right]}, \quad \frac{G_{\mathrm{SC}}}{G} = 1-\frac{32}{45}\frac{(1-\nu_{\mathrm{SC}})(5-\nu_{\mathrm{SC}})}{2-\nu_{\mathrm{SC}}}\eta, \tag{22}$$

where ν_{SC} is the effective Poisson ratio, K_{SC} and G_{SC} the effective bulk and shear moduli. The matrix's Poisson ratio ν, bulk and shear moduli K and G, are obtained from (20). The number of crack per unit volume is monitored by $0 \le \eta < \infty$ (Eq. 19). This method amounts to assume scale separation between the grains and a set of randomly-oriented cracks, at a higher length scale (see schematic view 8a).

We also consider the Mori-Tanaka estimate (Benveniste, 1987), equivalent to the "non-interacting approximation" (Kachanov, 1992) in which the effects of each crack on the compliance moduli are summed up, corresponding to a dilute approximation. These methods have been designed as a way to take into account "shielding effects" (Grechka and Kachanov, 2006), a situation that occurs when multiple nearby cracks cancel or reduce each other's softening effect. The estimates take the form:

$$\frac{K}{K_{\mathrm{NIA}}} = 1+\frac{16}{9}\frac{1-\nu^2}{1-2\nu}\eta, \qquad \frac{G}{G_{\mathrm{NIA}}} = 1+\frac{32}{45}\frac{(1-\nu)(5-\nu)}{2-\nu}\eta, \tag{23}$$

where $K_{\rm NIA}$ is the effective bulk modulus, $G_{\rm NIA}$ the effective shear modulus. The Poisson coefficient ν, and the elastic moduli G and K are obtained from (20), assuming scale separation. We denote this homogenization scheme (NIA).

We also combine Berryman's estimate (20) with the Hashin-Shtrikman-type bound (Ponte Castañeda and Willis, 1995):

$$\frac{K_{\rm HS}}{K} = 1 - \frac{48\eta(1-\nu^2)}{27(1-2\nu)+16\eta(1+\nu)^2}, \quad \frac{G_{\rm HS}}{G} = 1 - \frac{480\eta(1-\nu)(5-\nu)}{675(2-\nu)+64\eta(4-5\nu)(5-\nu)}, \tag{24}$$

which gives the bulk modulus $K_{\rm HS}$ and shear modulus $G_{\rm HS}$ of a cracked body as a function of the elastic shear modulus G, bulk modulus K and Poisson coefficient ν of the matrix. We denote (HS) the combination of the above formula with (20). Unlike methods (SC) and (NIA), formula (24) are exact upper-bounds for certain classes of materials containing randomly-oriented cracks with particular "ellipsoidal" form for the spatial correlations functions. For a cracked homogeneous body, the bounds require $\eta \leq 3/(4\pi) \approx 0.239$. This method does not provide bounds anymore when combined with Berryman's self-consistent estimate.

The self-consistent estimate proposed by Willot et al. (2018) for isotropic media containing cracks is also examined. This estimate reduces to a system of two cubic equations for the bulk and shear moduli of the cracked body, not recalled here for conciseness. Again, the bulk and shear moduli of the uncracked medium are provided by Berryman's estimate (20). This method is denoted (SC′-ISO).

In the dilute cracks-density limit $\eta \to 0$, the four methods (SC), (NIA), (SC′-ISO) and (HS) coincide up to first-order in η. This first-order correction is an exact result obtained for a set of isolated disk-shaped cracks embedded in a homogeneous, isotropic body (Kachanov, 1992). Except for method (NIA), all methods predict a (finite) percolation threshold in terms of the crack-density parameter η (we refer to Willot et al., 2018 for a discussion of percolation thresholds).

It is straightforward to extend methods (SC), (SC′-ISO), (NIA) and (HS) to thermal loadings. A general result states that the thermal expansion tensor of a homogeneous body is unchanged in the presence of pores (Rosen and Hashin, 1970). If scale separation between the grains and cracks is to be assumed, the effective thermal expansion coefficient $\widetilde{\alpha}_V$ does not depend on the crack density η. The value of $\widetilde{\alpha}_V$ for all three methods (SC), (SC′-ISO), (NIA) and (HS) is therefore provided by Eq. (21). In this equation, the value of $\widetilde{K}$ is given by Berryman's estimate for the uncracked polycrystal (Eq. 20). In the present case, the macroscopic thermal response depends on the density of cracks, because of the coupling between cracks and crystal anisotropy.

The self-consistent scheme developed for polycrystals with hexagonal symmetry containing cracks (Willot et al., 2018), denoted (SC′) hereafter, is also considered. Unlike methods (SC), (SC′-ISO), (NIA) and (HS), this approach does not assume scale separation between the grains and the cracks. Instead, cracks and grains are considered as inhomogeneities of similar size embedded in the effective medium (see schematic view 8b).

In the rest of this work we also use the upper and lower bounds $\alpha_V^{\pm}$ for the volumetric thermal expansion coefficient α_V available for microstructures with an arbitrary number of phases and triclinic anisotropy (Gibiansky and Torquato, 1997):

$$\begin{aligned}
\frac{\alpha_V^{\pm}}{3} &= \frac{B_2K_u(\widetilde{K}-K_m) - B_1(K_u-\widetilde{K}) \pm \sqrt{\Psi(\widetilde{K}-K_m)(K_u-\widetilde{K})}}{\widetilde{K}(K_u-K_m)}, \\
\Psi &= 2(C_1+C_2)(K_u-K_m) - B_1^2 - 2K_uB_1B_2 - K_mK_uB_2^2, \quad 9B_1 = -\langle\boldsymbol{\alpha}(\boldsymbol{x})\rangle : \mathbf{C}^a : \mathbf{I}, \\
3B_2 &= \langle\mathbf{C}(\boldsymbol{x}) : \boldsymbol{\alpha}(\boldsymbol{x})\rangle : \mathbf{S}^a : \mathbf{I}, \quad 18C_1 = \langle\boldsymbol{\alpha}(\boldsymbol{x}) : \mathbf{C}(\boldsymbol{x}) : \boldsymbol{\alpha}(\boldsymbol{x})\rangle - \langle\boldsymbol{\alpha}(\boldsymbol{x})\rangle : \mathbf{C}^a : \langle\boldsymbol{\alpha}(\boldsymbol{x})\rangle, \quad K_u = (\mathbf{I} : \mathbf{S}^a : \mathbf{I})^{-1} \\
18C_2 &= -\langle\boldsymbol{\alpha}(\boldsymbol{x}) : \mathbf{C}(\boldsymbol{x})\rangle : \mathbf{S}^a : \langle\boldsymbol{\alpha}(\boldsymbol{x}) : \mathbf{C}(\boldsymbol{x})\rangle, \quad \mathbf{C}^a = \langle\mathbf{S}(\boldsymbol{x})\rangle^{-1}, \mathbf{S}^a = \langle\mathbf{C}(\boldsymbol{x})\rangle^{-1}, \quad 9K_m = \mathbf{I} : \mathbf{C}^a : \mathbf{I},
\end{aligned} \tag{25}$$

where $I_{ij,kl} = (1/2)(\delta_{ik}\delta_{jl} + \delta_{il}\delta_{jk})$ is the fourth-rank unit tensor, δ the Kronecker delta symbol, and averages of $\mathbf{C}(\boldsymbol{x})$, $\mathbf{S}(\boldsymbol{x})$, $\boldsymbol{\alpha}(\boldsymbol{x})$ and of their tensorial products are taken over the spatial domain. The expressions above are readily computed for hexagonal polycrystals containing pores. Taking $\mathbf{C} = \mathbf{C}^{\rm H}$, $\boldsymbol{\alpha} = \boldsymbol{\alpha}^{\rm H}$, and pores with zero volume fraction (cracks), one obtains, after some algebra:

$$\alpha_V^{\pm} = \frac{3C^{\rm H}_{iikl}\alpha^{\rm H}_{kl}}{C^{\rm H}_{jjmm}} \pm |\alpha^{\rm H}_{33} - \alpha^{\rm H}_{11}|\sqrt{2}\left(\frac{C^{\rm H}_{11ii}C^{\rm H}_{33kk}}{C^{\rm H}_{jjmm}} - C^{\rm H}_{1133}\right)^{1/2}\left(\frac{1}{\widetilde{K}} - \frac{9}{C^{\rm H}_{jjmm}}\right)^{1/2}. \tag{26}$$

Fig. 9 illustrates the predictions of the bounds for the cracked hexagonal approximation of the TATB polycrystal (solid blue lines). Bounds for the hexagonal uncracked polycrystal (black line) reduce to Hashin's formula (21), whereas the bounds obtained for the uncracked polycrystal with triclinic anisotropy are represented in red. When cracks are present, the effective bulk modulus $\widetilde{K}$ takes on values ranging from 0 to Hill's upper bound. The

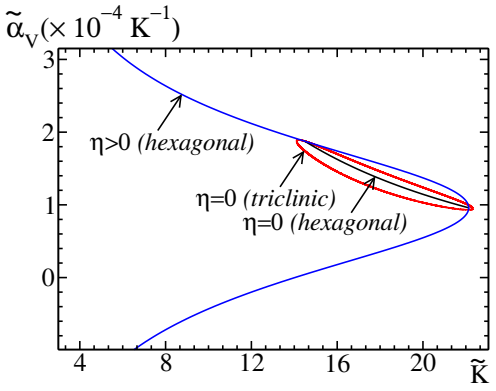

Figure 9: Effective thermal expansion coefficient $\widetilde{\alpha}_V$ as a function of the effective bulk modulus $\widetilde{K}$. Solid lines: Gibiansky and Torquato's upper and lower bounds (Gibiansky and Torquato, 1997) for the uncracked TATB polycrystal with triclinic anisotropy (red), Hashin formula (21) for hexagonal polycrystals (black), upper and lower bounds (26) for the cracked TATB polycrystal, with hexagonal approximation (blue).

difference between the upper and lower bounds for $\widetilde{\alpha}_V$ increases as the effective bulk modulus decreases. In the limit $\widetilde{K} \to 0$, the two bounds tend to $\pm\infty$. This behavior is similar to that obtained by Sigmund and Torquato (1997) for media made of pores and of two solid phases.

5 Thermoelastic response of cracked polycrystals: FFT results

5.1 Relative error: effect of voxel-discretization

In this section, we evaluate the accuracy of the FFT estimates of the effective properties of cracked polycrystals. Use is made of the "backward and forward" (FFT-BF) (Willot and Pellegrini, 2008) and "rotated" (FFT-R) (Willot, 2015) Fourier schemes. The reader is referred to our companion paper (Gasnier et al., 2018) for a discussion on the Fourier discretization schemes in media involving cracks. We consider the Johnson–Mehl model with transgranular cracks JM-T. The crack-density parameter η in model (JM-T) takes on 5 different values in the range [0.033; 0.35]. As shown in other works (Ambos et al., 2014, 2015; Gasnier et al., 2015b), the accuracy of the method for polycrystals without cracks is most influenced by the representativity of the microstructure, i.e. the number of grains. For models containing cracks however, the apparent moduli are sensitive to the thickness w of the cracks. This is especially true when dealing with random tessellations in 3D, where the cracks aspect ratio (thickness over length) cannot be as small as in ideal microstructures made of relatively few cracks.

The influence of w on the effective bulk moduli $\widetilde{K}$, $\widetilde{G}$ and thermal expansion coefficient $\widetilde{\alpha}_V$ is represented in Fig. 10 as a function of w. Symbols denote FFT data points with scheme FFT-BF (black signs) and FFT-R (colored symbols). Solid lines are linear fit of the FFT data points for $w \geq 2$. FFT results for the elastic moduli indeed show a linear decrease with respect to the thickness value $w \geq 2$ at fixed η (Figs. 10a and 10b). When $w = 1$ voxel, methods (FFT-R) and (FFT-BF) overestimate the elastic moduli. This is an effect of certain cracks that are ill-oriented with respect to the grid, and crudely discretized, allowing traction components to be partially transmitted across the crack. We refer to Gasnier et al. (2018) for a discussion of this effect for isolated cracks oriented parallel and transverse to the grid. Accordingly, we do not use the fine discretization $w = 1$ and choose $w = 2$. We also carry out all computations with (FFT-BF). The error estimate can be computed by comparing FFT numerical values for $w = 2$ and $w \to 0^+$, estimated by a linear fit for the FFT data point $w \geq 2$ (Fig. 10, solid black lines). The difference between the two values increases from 0.03% ($\eta = 0.033$) to 0.8% ($\eta = 0.35$) for $\widetilde{\alpha}_V$, from 1.1% ($\eta = 0.033$) to 15% ($\eta = 0.35$) for $\widetilde{G}$ and from 1.3% ($\eta = 0.033$) to 10% ($\eta = 0.35$) for $\widetilde{K}$. Elastic moduli are underestimated whereas the volumetric dilation coefficient is very slightly overestimated, due to the cracks finite thickness. Accordingly, except for the prediction of $\widetilde{\alpha}_V$ at low crack density values, the effect of the cracks's thickness discretization predominates over the volume representativeness. Note that, although the presence of voids or cracks does not influence the effective thermal expansion coefficient of a *homogeneous* body (Rosen and Hashin, 1970), this is not so, in general, for *inhomogeneous* bodies containing cracks such as polycrystals.

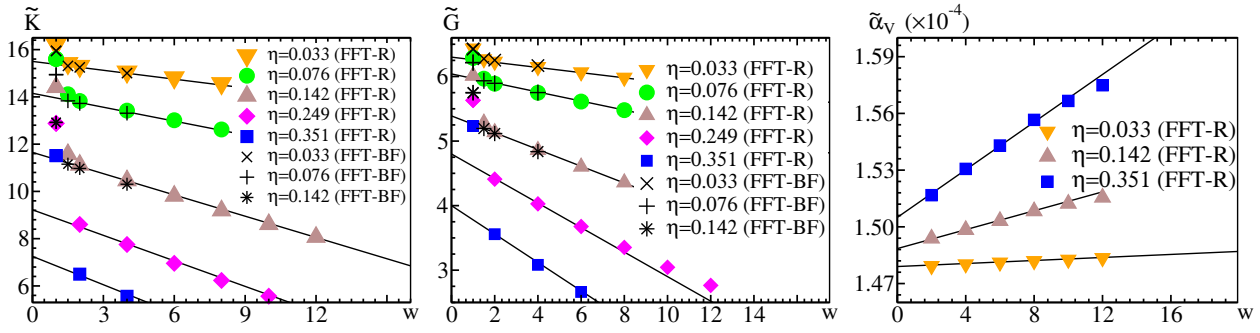

(a) (b) (c)

Figure 10: Influence of the crack width parameter w (in voxels unit length) on the effective elastic moduli (a-b) and thermal expansion coefficient (c) in a polycrystal (model JM-T) with transgranular cracks. Symbols: FFT data points using method FFT-BF (color symbols) and FFT-R (black signs), for various values of the crack density parameter η. Solid lines: linear fit in the range $w \geq 2$.

5.2 Intergranular vs. transgranular cracks

Results for the elastic moduli of models (V-I), (JM-I), (V-T) and (JM-T) are shown in Fig. 11. Solid lines of various colors represent the analytical estimates (NIA), (HS), (SC) and (SC′), whereas FFT data points are shown by symbols (green: intergranular cracks, black: transgranular cracks). It appears that all cracked media have the same bulk modulus in the dilute crack-density limit $\eta \ll 1$. Also, the analytical estimates, including (SC′), predict the same finite slope $\partial\widetilde{K}/\partial\eta$ at $\eta = 0^+$ (dotted line, embedded graph in Fig. 11a). The non-interacting approximation (NIA) gives the stiffest responses, which are not realistic for the transgranular and intergranular models. Methods (SC), (HS) and (SC′) provide a bulk modulus close to that obtained for the two transgranular models (JM-T) and (V-T), except at higher crack density ($\eta \geq 0.45$). In this regime, method (HS) predicts a softer response, at fixed η, than Fourier computations, for the transgranular models. Overall the tessellation model has a small impact on the bulk modulus, although Johnson–Mehl tessellations show stiffer properties than Voronoi's. For intergranular crack models, this effect is linked to the percolation threshold η_c of model (V-I), lower than that of model (JM-I). The values of the thresholds are about $\eta_c \approx 0.46$ (V-I) and $\eta_c \approx 0.61$ (JM-I) (Section 3.4). Likewise, models with transgranular cracks JM-T and V-T (black symbols), which do not exhibit a percolation threshold, have the stiffest response.

The situation is significantly different regarding the shear modulus (see Fig. 11b). The slope at $\eta = 0$ is about -33 GPa for intergranular and transgranular models (see embedded graph). This slope is quite lower than that given by methods (NIA), (HS) and (SC) which predict -9.3 GPa. Thus, contrarily to the bulk modulus case, crystal anisotropy has a weakening effect on the shear modulus in the dilute crack-density regime. Method (SC′) predicts a slope of about -15.1 GPa, and a weakening effect in the dilute regime due to crystal anisotropy. As expected, the value for the slope obtained by FFT is not recovered by (SC′), which does not take into account the exact local interaction between cracks and crystals. Nevertheless for crack density parameter in the range $0 \leq \eta \leq 0.6$, method (SC′) provides the best estimate for the shear modulus and the correct concavity.

The effective thermal expansion coefficient $\widetilde{\alpha}_V$ is represented in Fig. 12 as a function of the crack density η. When $\eta = 0$, $\widetilde{\alpha}_V$ is very close to the value 1.49×10^{-4} K^{-1} provided by Hashin's formula (Eq. 21). For the intergranular crack models (JM-T) and (V-T), the thermal expansion coefficient shows a slight increase with respect to η in the entire range $0 \leq \eta \leq 0.6$ (black symbols, Fig. 12). The same behavior is observed for intergranular cracks models (JM-I) and (V-I) up to $\eta \approx 0.3$. At higher crack density $\eta \geq 0.3$, a percolating behavior appears, highlighted by the strong increase of $\widetilde{\alpha}_V$ with respect to η (model JM-T, represented by green circles). This increase is not predicted by models (NIA), (SC) or (HS) (black solid line, Fig. 12). The self-consistent method (SC′) predicts an increase with respect to η while overestimating the effects of the cracks in the domain $\eta \leq 0.3$. At small crack density $\eta \leq 0.1$, the effects of cracks are amplified by a factor of about 2 by method (SC′) compared to FFT predictions (models V-T and V-I, embedded graph, Fig. 12). FFT data points for models (V-I) and (V-T) also suggest that the function $\widetilde{\alpha}_V$ is concave at moderate crack density $\eta \leq 0.3$, consistently with SC′. The bounds (26) (brown solid line, Fig. 12), give widely overestimated expansion coefficient $\widetilde{\alpha}_V$, but predict that $\widetilde{\alpha}_V$ is smaller than $\widetilde{\alpha}_V^{\mathrm{H}} \approx 1.87\,10^{-4}$ at $\eta = 0$.

The FFT point closest to the percolation threshold is found at $\eta \approx 0.56$ for model JM-I (Fig. 12). Contrarily

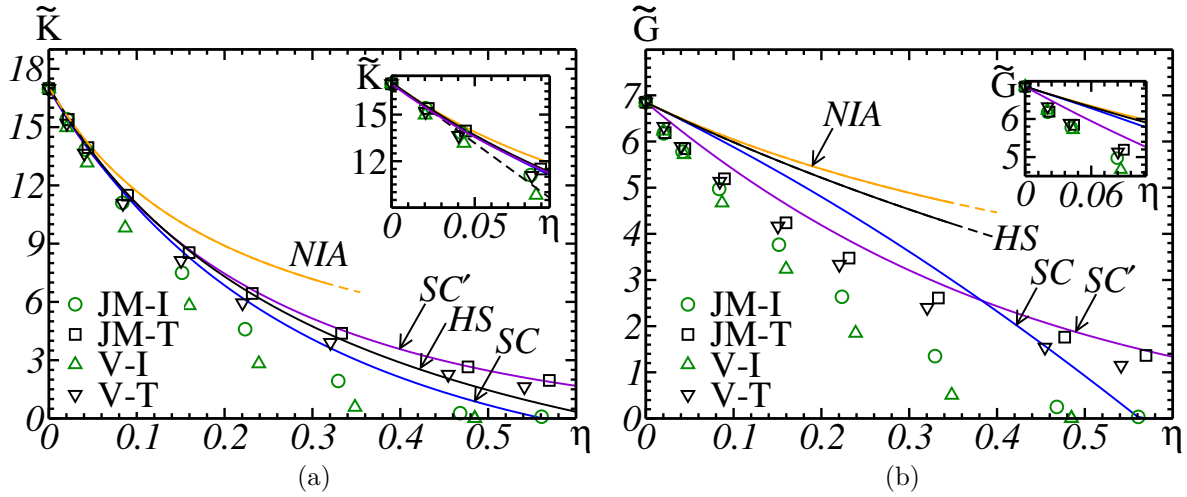

Figure 11: Bulk modulus $\widetilde{K}$ (a) and shear modulus $\widetilde{G}$ (b) of cracked polycrystals as a function of the crack density η. Symbols: FFT results for the Johnson–Mehl (JM, circles) and Voronoi tessellations (V, triangles) with intergranular (green) or transgranular cracks (black). Solid lines: linear homogenization theories. Orange: "non-interacting approximation" (NIA); Black: Hashin-Shtrikman-type bound (HS); Blue: self-consistent estimate for a homogeneous matrix (SC); Violet: self-consistent estimate for cracked hexagonal polycrystals (SC′); Top-right graphs (embedded): dilute crack density $\eta < 0.1$. Dashed line: tangent line for $\widetilde{K}$ at $\eta = 0$, common to SC, NIA and HS.

to other FFT data points, a single realization, rather than two realizations, is used here. The FFT estimate for the other realization was discarded because the crystals were found not to be connected. Indeed, the effective thermal expansion is estimated by the formula $\widetilde{\alpha}_V = -\overline{\sigma}_m/(\widetilde{K}\overline{\Delta T})$ which can not be used beyond the percolation threshold. FFT data for the effective thermal expansion coefficient of the non-percolating realization at $\eta \approx 0.56$ gives $\widetilde{\alpha}_V \approx 1.89 \times 10^{-4}$ K^{-1} which is close to $\alpha_V^{\mathrm{H}} \approx 1.88 \times 10^{-4}$ K^{-1}. It is notable that method SC′ predicts exactly $\widetilde{\alpha}_V \to \alpha_V^{\mathrm{H}}$ at percolation (Willot et al., 2018). Despite the very good agreement, however, additional numerical investigations are required to determine the exact nature of $\widetilde{\alpha}_V$ for integranular models in the percolation limit.

5.3 Effect of crystal anisotropy

The effect of crystal anisotropy is now examined taking advantage of the "binary" models (JM-IB) and (JM-TB) where the crystals have been replaced by the already-homogenized effective matrix. The effective thermal expansion coefficient of binary media predicted by FFT does not depend on η (not shown), consistently with the exact solution for binary media.

The effective bulk and shear moduli are represented in Fig. 13a and 13b, respectively, as a function of the crack density η. FFT data points for the binary models are represented with the symbols $\times$ (intergranular cracks) and $+$ (transgranular cracks). Binary microstructures have noticeably stiffer elastic moduli than their polycrystalline counterparts. The increase of the effective bulk modulus in particular is much more pronounced when intergranular cracks are concerned (see JM-I vs. JM-IB, Fig. 13a) than for transgranular cracks (JM-T vs. JM-TB, same figure). This is such that the bulk modulus of the binary model with intergranular cracks (JM-IB) is higher than with transgranular cracks (model JM-TB), whereas the order is reversed for non-binary models (JM-I) and (JM-T).

The concavity of the curves for the shear modulus $\widetilde{G}$ of the binary models (JM-IB) and (JM-TB) is much less pronounced than that of the polycrystal models (symbols $+$ and $\times$ vs. squares and circles, Fig. 13b). Also, the binary models display the same behavior in the dilute crack-density limit $\eta \to 0$ as that predicted by the estimates (NIA), (HS) and (SC) (embedded graph, Fig. 13b). This is not surprising as these homogenization schemes apply to binary media. Estimate (SC′) is represented in Fig. 13 as solid violet lines, and (SC′-ISO) as dotted violet lines.

5.4 Experimental vs. numerical results

Using FFT data points for models (JM-I) and (JM-T) (Fig. 11) we find the density of cracks in each model that allows one to recover the experimentally-observed bulk and shear moduli ($\widetilde{K} = 7.2$, $\widetilde{G} = 2.7$). For model (JM-I), on the one hand, we obtain similar crack density values $\eta = 0.18$ for $\widetilde{K}$ and $\eta = 0.24$ for $\widetilde{G}$. For model (JM-T), on the

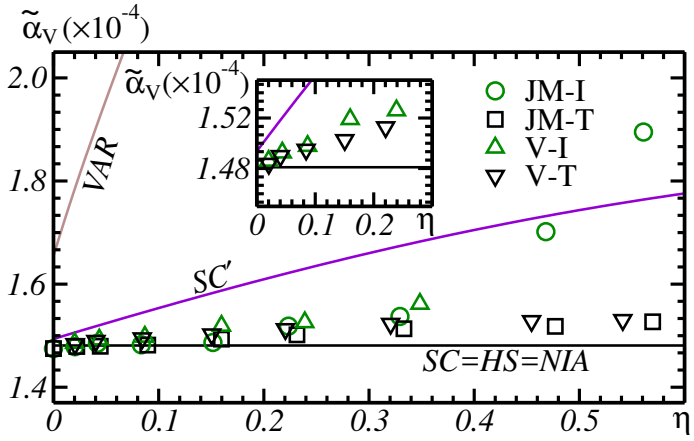

Figure 12: Continuation of Fig. 11: volumetric thermal expansion coefficient $\widetilde{\alpha}_V$. Embedded graph: enlargement in the region $\eta \leq 0.3$ for models (V-T) and (V-I), based on the Voronoi tessellation. Brown solid line: Gibiansky-Torquato upper-bound (VAR).

other hand, one has $\eta = 0.25$ for $\widetilde{K}$ and $\eta = 0.44$ for $\widetilde{G}$. Thus, model (JM-I), i.e. a material containing *intergranular cracks*, appears as the best candidate for modeling the TATB-based material in its initial state. FFT computations are also consistent with the measured volumetric thermal expansion coefficient $\widetilde{\alpha}_V = 1.45 \times 10^{-4}$ K^{-1}, although this value is not sensitive to the presence of cracks.

We emphasize that the FFT data overestimate the role of the cracks (see Section 5.1). Furthermore, the porosity and the binder are not taken into account. This rough analysis should be complemented by taking into account the weakening effects of both. Nevertheless, the results obtained so far cannot explain the decrease of the volumetric thermal expansion coefficient down to 1.02×10^{-4} K^{-1} observed under cooling (Table 2). In the next section, we explore additional models of cracked polycrystals in order to recover and interpret the experimental data.

6 Polycrystals with cracks correlated to crystallographic orientations

Correlations are now introduced between the cracks's directions and crystallographic orientations, in an effort to simulate more realistic models. Such correlations have been observed in alloys and metals for intergranular (Crawford and Was, 1992; Rath and Bernstein, 1971; King et al., 2008) as well as transgranular cracks (Bernstein, 1970). Transgranular cracks are considered in Section 6.1 and intergranular cracks in Section 6.2.

6.1 Transgranular crack models

Consider two models of transgranular cracks where cracks are oriented along the "weak-plane", i.e. normal to direction e_3 of the local TATB crystal (see Eq. 3), and, for comparison, a "stiff-plane" model where the normal to the cracks lies in the (e_1, e_2) plane. We denote the weak-plane model with Johnson–Mehl tessellation (JM-TW) and that with Voronoi tessellation (V-TW). The stiff-plane models are likewise denoted (JM-TS) and (V-TS).

Models (JM-TW) and (JM-TS) are generated as follows. First, a grain is picked randomly and uniformly among all grains. Second, a point is selected at random in the grain, uniformly in space. For voxelized microstructures, this is done by selecting a voxel in the grain, each voxel being assigned the same probability. In both models (JM-TW) and (JM-TS), the crack passes through the selected point. The normal to the crack is given by the lattice direction e_3 for weakest plane models. For stiff plane models, it is selected randomly and uniformly in a disc contained in the (e_1, e_2) plane. In contrast to the transgranular model (JM-T), cracks in models (JM-TS) or (JM-TW) are as likely to occur in large grains as they are in the smaller ones. However, cracks are not uniformly distributed inside a grain because of the method used to select a point. In grains with regular, nearly convex shape, cracks appear more frequently inside a central region. In addition, an analysis of the cracks configuration near the grains boundary show that none of the models (JM-TW), (V-TW), (JM-TS) or (V-TS) presents a percolation threshold for the polycrystalline matrix. Like previously, numerical computations are carried out using the FFT method on 512^3 voxel grids and apparent properties are averaged over two realizations. We refer to Fig. 14 for an example of a FFT computation with model (JM-TW). The same procedure is followed for the Voronoi tessellation (models V-TW and V-TS).

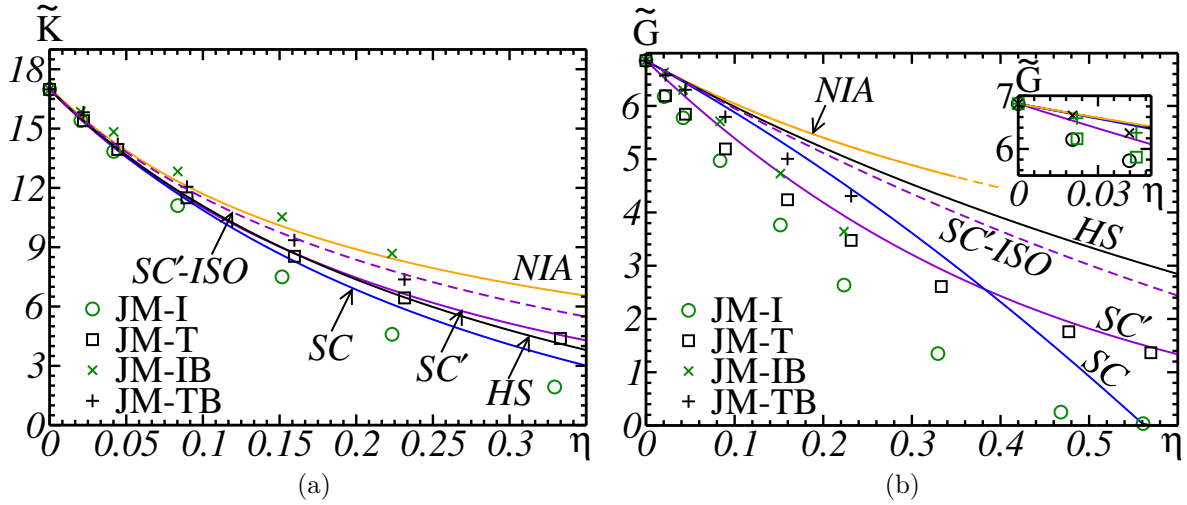

(a) (b)

Figure 13: Effect of crystal anisotropy on the bulk (a) and shear (b) moduli of cracked media. Squares and circles: FFT results for the Johnson–Mehl polycrystal with intergranular (green) and transgranular cracks (black); Signs (+) and (×): polycrystalline matrix replaced by an homogeneous isotropic medium. Solid lines: linear homogenization theories. Orange: non-interacting approximation (NIA); Black: Hashin-Shtrikman-type bound (HS); Blue: self-consistent estimate (SC); Violet: self-consistent estimate (SC′) for cracked hexagonal polycrystals. Dottted line: self-consistent estimate (SC′) in the case of isotropic grains, marked SC′ (ISO). Embedded graph (top-right): dilute crack density $\eta < 0.1$.

We also introduce a homogenization scheme relevant to the weak-plane model, which is given by the estimate for an uncracked polycrystal (Eq. 20) with the elastic moduli of the TATB replaced by transversely-isotropic grains that account for the presence of weak-plane cracks. These moduli are computed using the Eshelby tensor for an isolated penny-shaped crack embedded in a crystal with transversely-isotropic properties, and axis of symmetry normal to the crack, derived by Sevostianov et al. (2005). Accordingly, we replace the tensor components C^{H}_{ij} in Eq. (20) by the components of the following tensor:

$$\mathbf{C}^{\mathrm{TW}} = \left(\mathbf{S}^{\mathrm{H}} + \eta\mathbf{H}\right)^{-1}, \tag{27}$$

where $\mathbf{S}^{\mathrm{H}}$ is the hexagonal approximation of the compliance tensor of the TATB and $\mathbf{H}$ is given by (refering to the Voigt notation 3 and 4, with e_3 normal to the crack):

$$H_{33} = \frac{8}{3}\frac{\sqrt{C^{\mathrm{H}}_{33}\left(C^{\mathrm{H}}_{11}\right)^2/C^{\mathrm{H}}_{44} + 2C^{\mathrm{H}}_{11}\sqrt{C^{\mathrm{H}}_{33}C^{\mathrm{H}}_{11}} - C^{\mathrm{H}}_{13}C^{\mathrm{H}}_{11}\left(2 + C^{\mathrm{H}}_{13}/C^{\mathrm{H}}_{44}\right)}}{C^{\mathrm{H}}_{33}C^{\mathrm{H}}_{11} - \left(C^{\mathrm{H}}_{13}\right)^2}, \quad H_{66} = 2(H_{11} - H_{12}), \tag{28a}$$

$$H_{44} = H_{55} = \left(\frac{3}{16}\sqrt{C^{\mathrm{H}}_{66}C^{\mathrm{H}}_{44}} + \frac{\sqrt{C^{\mathrm{H}}_{11}/C^{\mathrm{H}}_{33}}}{2H_{33}}\right)^{-1}, \quad H_{11} = H_{22} = H_{12} = H_{13} = 0. \tag{28b}$$

The expression above is given by Sevostianov et al. (2005) in a slightly different form.

As in methods (SC), (NIA) or (HS), the thermal expansion coefficient $\widetilde{\alpha}_V$ relevant to (SC-TW) is estimated using Hashin's formula (21). In the polycrystal, each grain now contains a population of weak-plane microcracks at a small scale, hence, following (27), tensor $\mathbf{S}^{\mathrm{H}}$ is replaced by $\mathbf{S}^{\mathrm{H}} + \eta\mathbf{H}$ in (21). We denote this self-consistent estimate by (SC-TW). Method (SC-TW) assumes that the cracks are much smaller than the grains and oriented along the crystal weakest-plane in each grain, enhancing the crystal anisotropy (see Fig. 8c).

Numerical results for the elastic moduli are presented in Fig. 15. The weak and stiff transgranular models are compared to models (JM-T) and (V-T). As expected, FFT data points show a significantly stiffer response for the weak-plane model (black symbols in Fig. 15) than with other transgranular models (purple and orange symbols in Fig. 15). The stiff-plane model (orange symbols) yields elastic moduli that are very close to the uncorrelated models (JM-T) and (V-T) whereas the effect of the tessellation (JM vs. V) appears to be negligible. The bulk modulus $\widetilde{K}$ has a slightly different slope in the dilute crack density limit $\eta \to 0$ depending on the estimate. The self-consistent method (SC′) gives a slope of about -78.0 GPa whereas (SC-TW) predicts -109.0 GPa (note that the two curves cross each other at around $\eta = 0.09$, see Fig. 15a, embedded graph). FFT data for (JM-TW) and

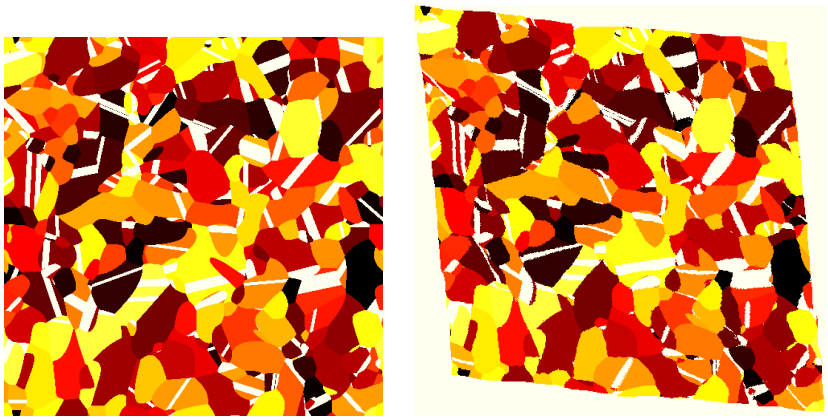

(a) (b)

Figure 14: Johnson–Mehl model with "weakest-plane" trangranular cracks (JM-TW) under shear loading $\bar{\varepsilon}_{xy} = \bar{\varepsilon}_{yx} = 10\%$: 2D cut along the (x, y)-plane of the undeformed (a) and deformed microstructure (b). Cracks in white, grains in yellow, orange, red and black.

(V-TW) do not predict such crossing, however recall that method (SC-TW) relies on the assumption that the cracks are entirely embedded in the same crystal which is not the case of the transgranular crack models.

To validate the numerical results, we carried out one additional FFT computation using a model similar to (JM-TW) with cracks diameter smaller by a factor 5 compared to the grains (model JM-TW′, black star in Fig. 15a), in an effort to generate a structure closer to that represented in Fig. 8c. We also computed the same estimate as (SC-TW) for ellipsoidal voids that mimic cracks with finite thickness. This is done by replacing, in method (SC-TW), the tensor $\mathbf{H}$ (Eq. 27) by a formula valid for ellipsoids with finite thickness, provided by Sevostianov et al. (2005). This expression is not provided here for conciseness. The volume fraction of the ellipsoid is chosen equal to that used in the numerical computation. The curve is marked (SC-TW′) in Fig. 15a. It presents nearly the same slope at $\eta = 0$ as the estimate (SC-TW). Also, the FFT data point for (JM-TW′) lies very close to the curve (SC-TW′). This result shows that the difference observed between the FFT predictions for model (JM-TW) or (V-TW) and the self-consistent estimate (SC-TW) can be attributed to two factors: the finite cracks thickness in the FFT computations and the scale separation hypothesis in (SC-TW).

Results for the shear modulus (Fig. 15b) are similar to that obtained for the bulk modulus. The weak-plane models (JM-TW) and (V-TW) exhibit the stiffest response. Self-consistent estimates present similar slopes at $\eta = 0$ for the weak-plane model SC-TW (-16.2 GPa) and for the transgranular model SC′ (-15.8 GPa) (embedded graph, Fig. 15b). However, no crossing is observed for the two estimates.

The effective thermal expansion coefficient is plotted as a function of the crack density parameter in Fig. 16, for all transgranular models. As for the bulk modulus, we compare the FFT prediction for model (JM-TW′) with the self-consistent estimate (SC-TW′). The difference between the FFT result for (JM-TW′) and method (SC-TW′) diminishes significantly compared to (JM-TW) and (SC-TW), validating our approach.

Data obtained for $\widetilde{\alpha}_V$ show that the thermal expansion coefficient is sensitive to the orientation of the cracks with respect to the crystallographic lattice. Specifically, $\widetilde{\alpha}_V$ decreases when the density of transgranular cracks oriented along the weak-plane of the TATB crystal increases (black symbols, Fig. 16). Conversely, stiff-plane cracks induce an increase of the thermal expansion coefficient with respect to η (orange symbols). This behavior can be interpreted using Hashin's formula (21), which reads, for model (SC-TW):

$$\widetilde{\alpha}_V = 3\alpha^{\mathrm{H}}_{11} + (\alpha^{\mathrm{H}}_{33} - \alpha^{\mathrm{H}}_{11})\frac{1/\widetilde{K} - 3S^{\mathrm{H}}_{ii11}}{S^{\mathrm{TW}}_{ii33} - S^{\mathrm{H}}_{ii11}}, \qquad S^{\mathrm{TW}}_{ii33} = S^{\mathrm{H}}_{ii33} + H_{33}\eta, \tag{29}$$

where, for the uncracked TATB, $1/\widetilde{K} - 3S^{\mathrm{H}}_{ii11} > 0$, $S^{\mathrm{TW}}_{ii33} - S^{\mathrm{H}}_{ii11} > 0$ and $\alpha^{\mathrm{H}}_{33} - \alpha^{\mathrm{H}}_{11} > 0$. Assume that the variations of $\widetilde{K}$ with respect to η can be neglected. Weak-plane cracks increase the anisotropy of the crystal, represented by the denominator $S^{\mathrm{TW}}_{ii33} - S^{\mathrm{H}}_{ii11}$ of the second term on the r.h.s., lowering $\widetilde{\alpha}_V$. The opposite effect is observed for stiff-plane cracks, where the grains anisotropy is diminished.

FFT results for weak-plane transgranular cracks at $\eta \approx 0.7$ is consistent with volumetric thermal expansion data as low as 1.11×10^{-4} K^{-1}, measured during re-heating (Table 2). The lowest value 1.02×10^{-4} K^{-1} requires possibly larger crack density $\eta > 0.7$ that are difficult to compute numerically.

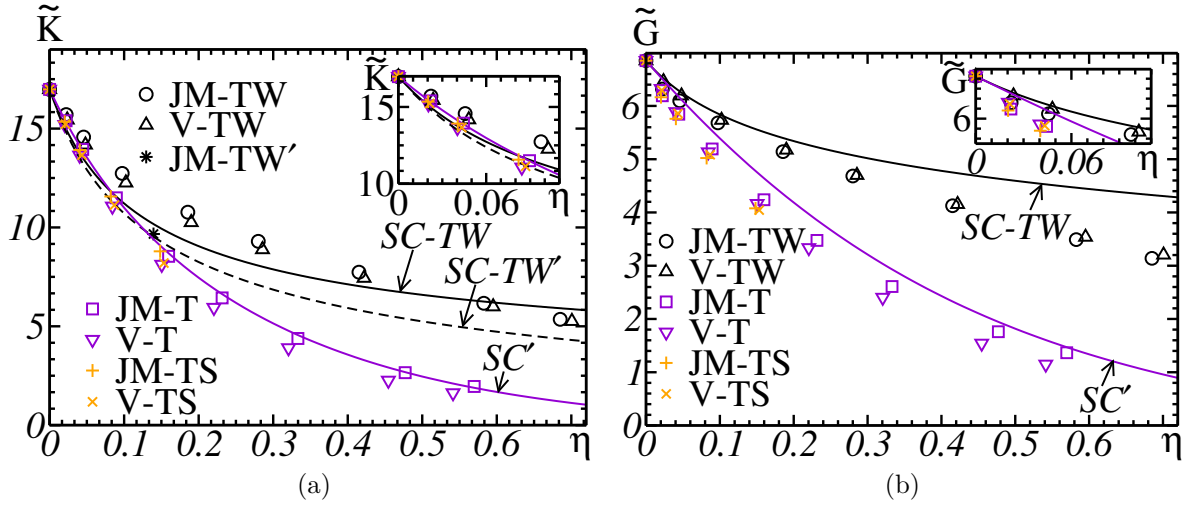

Figure 15: Elastic moduli of weak-plane (black symbols) and stiff-plane (orange symbols) transgranular crack models, as a function of the crack density parameter η, and compared to uncorrelated transgranular models (purple symbols). Solid lines: self-consistent estimates (SC-TW), (SC-TW′) relevant to weak-plane cracked models and (SC′). Embedded graphs: enlargement around small crack density.

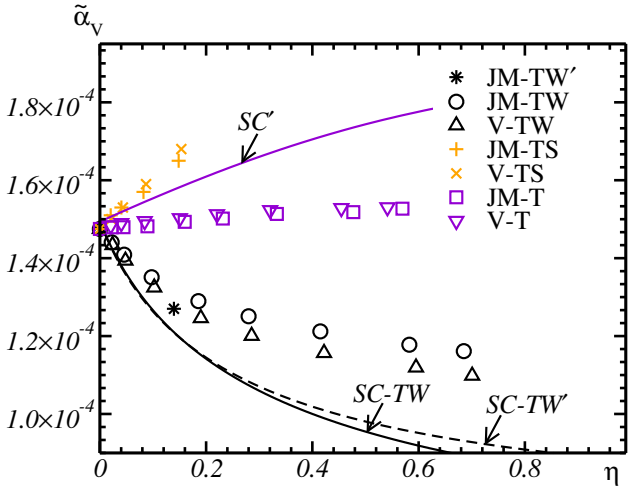

Figure 16: Continuation of Fig. 15: volumetric thermal expansion coefficient $\widetilde{\alpha}_V$.

We now determine the limiting behavior of $\widetilde{K}$ and $\widetilde{\alpha}_V$ when $\eta \to \infty$, predicted by method (SC-TW). We rewrite Eqs. (20) in terms of the in-plane and out-of-plane Young moduli E_p and E_z of the hexagonal approximation of the TATB crystal, the in-plane shear modulus G_{zp} and the Poisson ratios ν_p and ν_{pz} (Eq. 15). Weak-plane transgranular cracks lower the moduli G_{zp} and E_z while leaving E_p and Poisson ratios intact. An asymptotic expansion of the estimate for (SC-TW) when $G_{zp} \to 0$ and $E_z \to 0$ leads to:

$$\widetilde{K} \sim \frac{4}{3}\widetilde{G} \sim \sqrt{\left(3E'_z + 16G'_{zp}\right)\frac{2E_p}{9(7+\nu_p)}}, \tag{30}$$

where:

$$G'_{zp} = \left(\frac{1}{G_{zp}} + \eta H_{44}\right)^{-1}, \qquad E'_z = \left(\frac{1}{E_z} + \eta H_{33}\right)^{-1}, \tag{31}$$

are the shear moduli and Young moduli weakened by the presence of transgranular cracks, obtained from (28) and (27). For the TATB, $H_{33} \approx 0.63$ GPa^{-1} and $H_{44} \approx 0.42$ GPa^{-1}. Thus, when $G'_{zp} \ll E'_z$, $\widetilde{K}$ scales as:

$$\widetilde{K} \sim \sqrt{\frac{2E_p}{3H_{33}(7+\nu_p)}}\frac{1}{\sqrt{\eta}} + \mathcal{O}(1/\eta). \tag{32}$$

The above regime holds in the region $\eta_0 \ll \eta \ll \eta_1$ with:

$$\eta_0 = \frac{1}{E_z H_{33}}, \qquad \eta_1 = \frac{1/G_{zp} - 1/E_z}{H_{33} - H_{44}}, \tag{33}$$

where we assumed that $H_{33} > H_{44}$ as is the case for the TATB. When $\eta \gg \eta_1$, $E'_z/G'_{zp} \approx H_{44}/H_{33}$ and:

$$\widetilde{K} \sim \sqrt{\left(\frac{3}{H_{33}} + \frac{16}{H_{44}}\right) \frac{2E_p}{9(7+\nu_p)}} \frac{1}{\sqrt{\eta}} + \mathcal{O}(1/\eta), \qquad . \tag{34}$$

For the TATB crystal, there is less than two decades between $\eta_0 \approx 0.09$ or $\eta_1 \approx 4.2$, and regime (32) does not occur. It is nevertheless visible as an inflexion point when $\widetilde{K}$ is plotted as a function of η in log-log plot (Fig. 17, solid blue line). To highlight this regime we have computed estimates of $\widetilde{K}$ predicted by method (SC-TW) for a crystal with amplified anisotropy (solid black line). This crystal has the same moduli as that of the TATB except that G_{zp} is one hundred times smaller (equal to 0.0104 GPa). For this material, $\eta_0 \approx 0.009$, $\eta_1 \approx 47$ and the two regimes (32) and (34) distinctly appear (Fig. 17, red and green dotted lines). Making use of (29), we obtain the limiting behavior of $\widetilde{\alpha}_V$ when $\eta \to \infty$:

$$\widetilde{\alpha}_V = 3\alpha_{11}^{\mathrm{H}} + \frac{\alpha_{33}^{\mathrm{H}} - \alpha_{11}^{\mathrm{H}}}{\sqrt{\eta}} \times \begin{cases} \sqrt{\frac{3(7+\nu_p)}{2E_p H_{33}}}, & \eta_0 \ll \eta \ll \eta_1, \\ \sqrt{\frac{9(7+\nu_p)}{2E_p(16H_{33}^2/H_{44}+3H_{33})}}, & \eta_1 \ll \eta, \end{cases} \tag{35}$$

The two regimes determined previously for $\widetilde{K}$ appear in the next-to-leading order term for $\widetilde{\alpha}_V$. The limiting value $\widetilde{\alpha}_V \to 3\alpha_{11}^{\mathrm{H}}$ as $\eta \to \infty$ in (35) is confirmed by the exact relationship (Benveniste, 1993):

$$\widetilde{\boldsymbol{\alpha}} : \langle \boldsymbol{\sigma}(\boldsymbol{x}) \rangle = \langle \boldsymbol{\alpha}^{\mathrm{H}}(\boldsymbol{x}) : \boldsymbol{\sigma}(\boldsymbol{x}) \rangle, \tag{36}$$

valid for purely-elastic loading ($\overline{\Delta T} = 0$). Indeed, let $\sigma_{33} \approx 0$ in grains with symmetry axis e_3 so that the traction component normal to the crack vanishes. The r.h.s. of (36) then reads:

$$\langle \boldsymbol{\alpha}^{\mathrm{H}}(\boldsymbol{x}) : \boldsymbol{\sigma}(\boldsymbol{x}) \rangle = 3\alpha_{11}^{\mathrm{H}} \overline{\sigma}_m = \widetilde{\alpha}_V \overline{\sigma}_m,$$

the material being subjected to hydrostatic stress loading $\overline{\sigma}_{ij} = \overline{\sigma}_m \delta_{ij}$. Likewise, in a grain containing many stiff-plane cracks oriented parallel to e_3 (models V-TS and JM-TS), the stress components σ_{11} and σ_{22} approach zero. A similar reasoning suggests the limiting value $\widetilde{\alpha}_V \to 3\alpha_{33}^{\mathrm{H}}$ as $\eta \to \infty$ for the stiff-plane crack models (V-TS) and (JM-TS). Remark that the limiting value $\widetilde{\alpha}_V \to \alpha_V^{\mathrm{H}}$ predicted by the self-consistent estimate SC′ for random crack orientations (see Willot et al., 2018) lies in-between $3\alpha_{11}^{\mathrm{H}}$ and $3\alpha_{33}^{\mathrm{H}}$, so that the thermal response of a mixture of randomly-oriented cracks is intermediate between that obtained for weak-plane and stiff-plane cracks.

For comparison purposes, FFT computations on a Voronoi polycrystal with the elastic moduli $\mathbf{C}^{\mathrm{TW}}$ in the grains have been carried out, for crystals with amplified anisotropy (purple stars, Fig. 17). As in the self-consistent estimate (SC-TW), the crystal's anisotropy is increased to mimic the presence of weak-plane microcracks. The FFT data points are very close to the (SC-TW) estimate (solid black line, Fig. 17) up to about $\eta \approx 2$, in-between the two regime changes predicted by (SC-TW). Yet they exhibit a different behavior than predicted by (SC-TW) for $\eta \gg \eta_1$, namely, the effective bulk modulus tends to the finite value $\widetilde{K} \approx 1.8$ GPa, whereas the effective shear modulus tends to the finite value $\widetilde{G} \approx 1.2$ GPa when $\eta \to \infty$.

Keeping $\widetilde{K}$ finite in Hashin's formula (21) and using (31), one obtains the same limiting value $\widetilde{\alpha}_V \to 3\alpha_{11}^{\mathrm{H}}$ when $\eta \to \infty$ as predicted by (SC-TW). However, the next-to-leading order term decreases as $1/\eta$ instead of $1/\sqrt{\eta}$ as predicted by SC-TW (Eq. 35).

6.2 Intergranular cracks

In this section, we explore various intergranular crack models that, unlike models (JM-I) and (V-I), contain correlations between the crack orientations and that of the surrounding crystals. More specifically, we try to reproduce the results obtained for $\widetilde{\alpha}_V$ in Section 6.1 for weak-plane cracks using intergranular cracks. The situation is more complicated for intergranular cracks where three local directions are present: the symmetry axis of the two grains adjacent to the crack and the orientation of the grain boundary.

Two types of correlated intergranular cracks are introduced. In the first model, intergranular cracks are placed along faces between adjacent grains with highest misorientations, irrespective of the grain boundary orientation. This model is denoted (JM-IM) and (V-IM), for the Johnson–Mehl and Voronoi tessellations, respectively. The

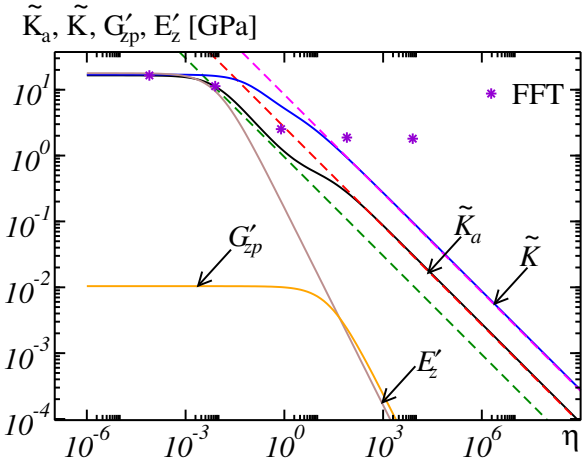

Figure 17: Effective bulk moduli of polycrystals with hexagonal symmetry. The grains's anisotropy mimics the presence of intragranular cracks oriented along the "weakest-plane" and the bulk moduli are plotted as a function of the crack density η. Solid lines: self-consistent estimate (SC-TW) for the bulk modulus $\widetilde{K}$ of the TATB polycrystal (blue) and for the bulk modulus $\widetilde{K}_a$ of a polycrystal with amplified anisotropy compared to the TATB (black, see text). Brown: out-of-plane Young modulus E'_z in grains with amplified anisotropy, provided by the non-interacting approximation (Sevostianov et al., 2005) and used in method (SC-TW). Orange: in-plane shear modulus G'_{zp}. Dotted lines: asymptotic expansions (32) (green) and (34) (red) for $\widetilde{K}_a$ and expansion (34) for $\widetilde{K}$ (magenta). Stars: FFT data points for the bulk modulus $\widetilde{K}_a$ of the polycrystal with amplified anisotropy.

second model of intergranular cracks is opposite to (JM-IM) and (V-IM), in the sense that cracks are placed when the misorientation between the two axis of symmetries of the surrounding crystals is small, and when the normal of the boundary coincides with that direction. Accordingly, cracks in this model can be thought of as reproducing the weak-plane model (V-TW) for intergranular cracks. This model is denoted (V-IC) and referred to as "correlated model of intergranular cracks". For simplicity, only the Voronoi tessellation is considered. Note that contrarily to model (V-IC), the cracks orientation with respect to crystallography is not taken into account in models (JM-IM) and (V-IM).

For simulating intergranular cracks along misoriented grains (models JM-IM and V-IM), we order the faces from the highest to the lowest misorientation of their respective adjacent grains. Cracks are placed in the order of misorientation, starting from the highest value. For models (JM-IM) and (V-IM) the misorientation is the angle between the symmetry axis of the two adjacent grains. For models (JM-IC) and (V-IC), faces are ordered from the lowest misorientation to the highest. The misorientation is the highest angle between any two axis among the normal to the grain boundary and the axis of symmetry of the adjacent grains.

The elastic moduli for models (JM-IM) and (V-IM) show almost no difference with that of the uncorrelated intergranular models (JM-I and V-I) (see Fig. 18, red and black symbols respectively). Model (JM-IM) displays slightly stiffer effective moduli than model (V-I), like the uncorrelated models (JM-I) which shows a stiffer response than (V-I) (Fig. 11). Our data indicates that the two models (JM-IM) and (V-IM) are also very close to (JM-I) and (V-I) in terms of thermal expansion coefficient (Fig. 19). However, a decrease of the thermal expansion coefficient $\widetilde{\alpha}_V$ with respect to the crack density is obtained for the model (V-IC) (Fig. 19, blue symbols). This result confirms that correlations between the cracks and the crystallographic orientations lead to a decrease of the thermal expansion coefficient. This behavior is observed when cracks are oriented along the weakest plane in the local crystal (models JM-TW and V-TW) or along crystal boundaries that are parallel to the crystals's weakest planes (model V-IC). Yet, model (V-IC), contrarily to the misoriented models (V-IM) and (JM-IM) is difficult to justify from a physical point of view, unless strong differences in grain-grain or grain-binder adhesion with TATB plane orientation be invoked, as suggested by Xiao et al. (2005). At this point the presence of intergranular cracks oriented along the weak-planes of the crystal (model JM-TW) appears as the most likely candidate for interpreting the decrease of $\widetilde{\alpha}_V$ obtained experimentally.

Although this study has focused on effective properties, it is worth emphasizing that the local fields are very sensitive to the cracks spatial distribution. Fig. 20 shows histograms for the strain component $\varepsilon_{xx}(\boldsymbol{x})$ in the connected component of the grains for five Johnson–Mehl tesselations with crack density $\eta = 0.24$: (JM-IB), (JM-TS), (JM-T), (JM-I) and (JM-TW) and for the uncracked Johnson–Mehl tesselation (JM). Hydrostatic strain loading $\langle \varepsilon_m \rangle = 100\%$ is applied. For cracked media, the histograms present a cusp at $\varepsilon_{xx} = 0$ (incrusted graph,

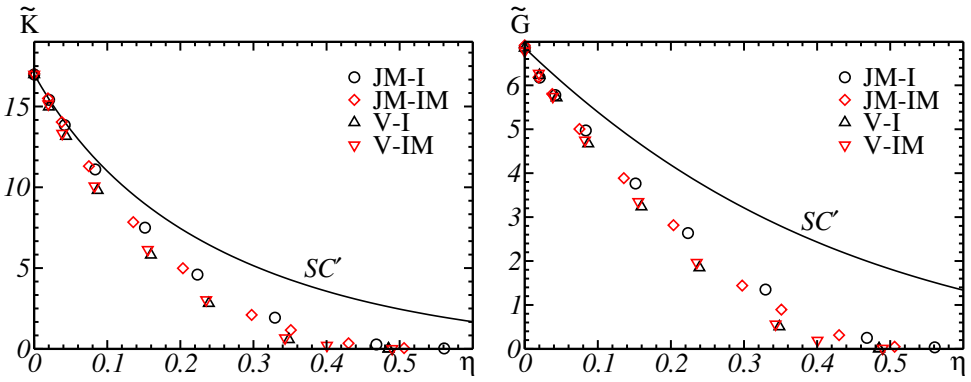

(a) (b)

Figure 18: Bulk modulus $\widetilde{K}$ (a) and shear modulus $\widetilde{G}$ (b) of polycrystals with intergranular cracks as a function of the crack density η. Black symbols: the presence of a crack is not correlated to the adjacent grains orientations; Red: cracks occur in-between misoriented grains. Circles and diamonds: Johnson–Mehl tessellation; triangles: Voronoi tessellation. Solid line: self-consistent estimate SC′ for cracked hexagonal polycrystals.

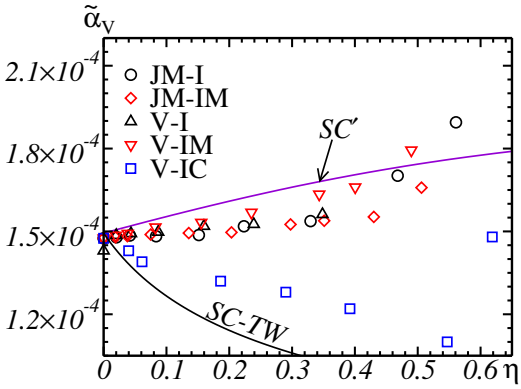

Figure 19: Continuation of Fig. 18: volumetric thermal expansion coefficient $\widetilde{\alpha}_V$. Squares: Voronoi tessellation with "correlated" intergranular cracks model (V-IC).

top-left), whose study is beyond the scope of the present work.

7 Discussion

The most prominent result of this numerical study is that the elastic effective moduli decrease systematically and monotonically with the density of any kind of microcracks, but that this is not the case for the effective thermal expansion coefficient. The latter is unaffected if microcrack orientations are not correlated with crystallographic ones, irrespective of the nature of microcracks (i.e. inter or transgranular).

A first conclusion can be drawn about the material in its initial state. We reported bulk and shear moduli much lower than those of the perfect polycrystal, but nearly identical expansion coefficients (see Section 2). The first finding indicates that microcracks are present in the material, and the second that they *must be uncorrelated to the crystal orientation*.

The results show that it is possible to find a single microcrack density that allows matching elastic and thermal expansion effective properties to experimental ones, but only in the case of intergranular microcracks. This density is close to 0.2 in the Budiansky definition. Therefore, the second conclusion is that the material contains a population of *uncorrelated intergranular microcracks* in its initial state, in other words that the polycrystal is imperfectly bonded.

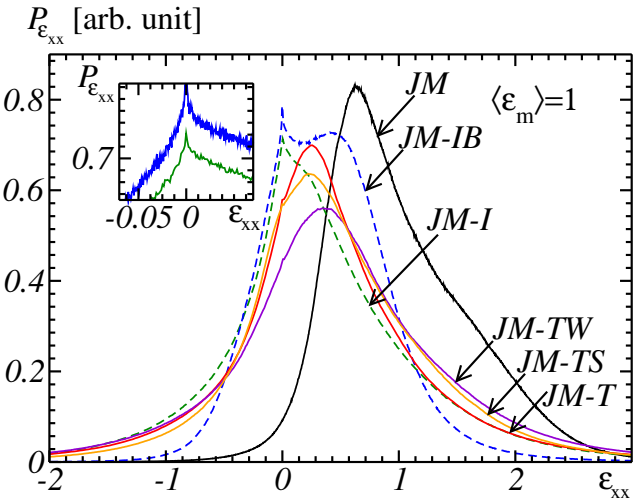

Figure 20: Histograms of the component ε_{xx} in various cracked Johnson–Mehl models (colored curves) with $\eta = 0.24$ and in an uncracked model (black solid line). Embedded graph: enlargement around $\varepsilon_{xx} \approx 0$ for models JM-IB and JM-I.

Concerning the effect of thermal loading on the expansion coefficient, several conclusions may be drawn. First, the only two candidate mechanisms inducing a decrease of the expansion coefficient are transgranular microcracking along the graphitic planes of the TATB crystal and "correlated" intergranular debonding between grains of similar orientations. Therefore, low-temperature damage is likely to follow one of these mechanisms.

In order to provide some experimental support to the above-described scenarios, a sample was cooled to −100 °C during 24 h, then heated back to ambient temperature, cut and polished. An exploratory post-mortem investigation using scanning electron microscopy was then conducted. Fig. 21 is an example of result, in which some of the TATB grains display embedded arrays of parallel transgranular cracks, compatible with the correlated transgranular microcracking scenario put forward above. Note that this is only an exploratory finding, that should not be considered as definite. More involved observations are being conducted at present, including comparisons with a fresh sample of the same batch. Also note that microcracks induced by the thermal load must close back under thermal load removal, explaining the faint appearance of cracks in Fig. 21, in which the contrast is already artificially enhanced. We were even able to monitor crack closure under the heating action of the electron beam. Besides, intergranular cracks are quite difficult to discriminate from usual grain boundaries, so that no conclusion can be drawn for this microcracking process. The only way to provide definite conclusions is to perform in situ observations, i.e. *during cooling*. Such experiments are presently being designed and will be reported later.

Second, the damage process observed at high temperature but below the glass transition must be uncorrelated microcracking since it induces no significant variation of the expansion coefficient. An uncorrelated transgranular microcracking process appears unlikely, due to the difference between in-plane and out-of-plane molecular bond strengths. Therefore, an intergranular uncorrelated microcracking process, i.e. debonding, is the most likely candidate mechanism for this temperature range.

Third, crossing the glass transition temperature involves a dramatic decrease of the mechanical strength of the binder, and even melting. Thus, on the one hand, no more stress is sustained by the material, and transgranular cracking cannot occur. On the other hand, binder melting is equivalent, as a first approximation, to vanishing of all intergranular strength, and the material behaves as a fully intergranular microcracked (or comminuted) material. From a macroscopic viewpoint, this is equivalent to the situation when microcrack percolation occurs, with accompanying bulk and shear moduli vanishing, and explains the increase of the expansion coefficient.

At this stage, the question of thermal expansion input data must be raised. All the preceding discussion assumes that the single crystal thermal expansion data of Sun et al. (2010) are correct. Consider now the case where the data of Kolb and Rizzo (1979) would be the correct ones. Then, the expansion coefficient of the perfect polycrystal would be 2.44×10^{-4} K $^{-1}$ (Gasnier et al., 2015b), and the initial material could only contain weak plane transgranular microcracks to retrieve the measured expansion coefficient. It would involve very large microcrack densities, and much too low corresponding effective elastic properties. This scenario is therefore unlikely, which explains why the

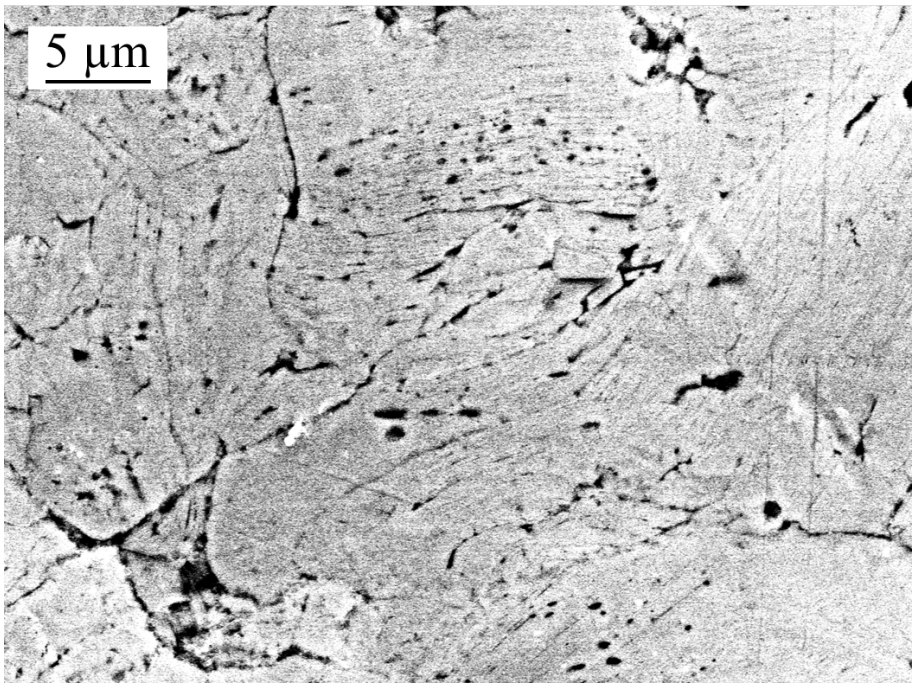

Figure 21: Example of scanning electron micrograph of a sample submitted to a thermal load to $-100°C$ during 24 hours, heated back to ambient temperature, vacuum impregnated with an epoxy resin, cut, polished and observed with no metallization. Most of the grains appear foliated, containing very thin parallel lines (see blue line stacks), consistent with intra- or transgranular microcracks lying in the graphitic plane of the grains. Notice that these thin lines are parallel but not straight, which is attributed to the twin-like bands observed in most grains under polarized light optical microscopy (see Ambos et al., 2015).

data in Kolb and Rizzo (1979) were discarded in the present work.

8 Conclusion

The proposed heuristic methodology allows one to infer microcrack location from experimental data, especially thermal loading cycles in similar polycrystals. More precisely, the crystal should have hexagonal anisotropy and strongly different thermal dilation coefficients in directions transverse or parallel to the plane of symmetry.

This study also shows that the nature of the cracks, either intergranular or transgranular, with orientations parallel to the weak-plane in the crystal or random, yields quite different elastic moduli. The interplay between crystal anisotropy and cracks can be accounted for, to some extent, by the self-consistent homogenization scheme deviced for cracked polycrystals, when dealing with transgranular cracks with orientations uncorrelated to the crystals. Analytical estimates are however unable to account for the full interaction between a crack and adjacent grains, typically intergranular cracks, in contrast with full-field computations.

Acknowledgments

The authors are indebted to Didier Picart, Jean-Luc Brigolle and Christophe Pompon for providing the uniaxial compression data, to Philippe Bortoluzzi and Alain Fanget, who performed the triaxial compression experiments, to Alexandre Forzy, Alexandre Lecardeur and Pascal Palmas, who prepared the samples and performed the scanning electron microscopy observations, and to Carole Nadot-Martin for useful suggestions. The authors also gratefully acknowledge the financial support of the French Commissariat à l'Énergie Atomique.

References

Ambos A., Trumel H., Willot F., Jeulin D. and Biessy M., A fast Fourier transform micromechanical upscaling method for the study of the thermal expansion of a TATB-based pressed explosive, In: Proceedings of the 15$^{\text{th}}$

International Detonation Symposium, San Francisco, CA, July 13-18, 2014, online at https://hal.archives-ouvertes.fr/hal-1097110.

Ambos A., Willot F., Jeulin D. and Trumel H., Numerical modeling of the thermal expansion of an energetic material, *Int. J. Solids Struct.* **60–61**, 2015, 125–139.

Bedrov D., Borodin O., Smith G.D., Sewell T.D., Dattelbaum D.M. and Stevens L.L., A molecular dynamics simulation study of crystalline 1,3,5-triamino-2,4,6-trinitrobenzene as a function of pressure and temperature., *J. Chem. Phys.* 131, 2009, 224703.

Benveniste Y., A new approach to the application of Mori-Tanaka's theory in composite materials, *Mech. Mater.* **6** (2), 1987, 147–157.

Benveniste Y., Universal relations in piezoelectric composites with eigenstress and polarization fields, Part 2: Multiphase media–effective behavior, *J. Appl. Mech.* **60** (2), 1993, 270–274.

Bernstein I.M., The role of hydrogen in the embrittlement of iron and steel, *Mater. Sci. Eng.* **6** (1), 1970, 1–19.

Berryman J.G., Bounds and self-consistent estimates for elastic constants of random polycrystals with hexagonal, trigonal, and tetragonal symmetries, *J. Mech. Phys. Solids* **53** (10), 2005, 2141–2173.

Budiansky B. and O'Connell R.J., Elastic moduli of a cracked solid, *Int. J. Solids Struct.*, **12** (2), 1976, 81–97.

Cady H.H. and Larson A.C., The crystal structure of 1,3,5-Triamino-2,4,6-Trinitrobenzene, *Acta Crystall.* 18, 1965, 485–496.

Crawford D.C. and Was G.S., The role of grain boundary misorientation in intergranular cracking of Ni-16Cr-9Fe in 360°C argon and high-purity water, *Met. Trans. A* **23** (4), 1992, 1195–1206.

Dallman J.C. and Wackerle J., Temperature-dependent shock initiation of TATB-based high explosives, In: Proceedings of the 10$^{\text{th}}$ International Symposium on Detonation, 1993, Boston, MA; USA.

Delannay L., Yan P., Payne J.F.B. and Tzelepi N., Predictions of inter-granular cracking and dimensional changes or irradiated polycrystalline graphite under plane strain, *Comput. Mat. Sci.* 87, 2014, 129–137.

Ferenc J.-S. and Néda Z., On the size distribution of Poisson Voronoi cells, *Phys. A: Stat. Mech. Appl.* 385, 2007, 518–526.

Gasnier J.-B., Figliuzzi B., Faessel M., Willot F., Jeulin D. and Trumel H., 2015a. 3D morphological modeling of a polycrystaline microstructure with non-convex, anisotropic grains. Acta Stereologica: Proceedings of the 14$^{\text{th}}$ International Congress of Stereology and Image Analysis (ICSIA), Liège, July 7-10, online at https://hal.archives-ouvertes.fr/hal-01184811.

Gasnier J.-B., Willot F., Trumel H., Figliuzzi B., Jeulin D. and Biessy M., A Fourier-based numerical homogenization tool for an explosive material, *Matériaux Techn.* **103** (3), 2015, 308.

Gasnier J.-B., Willot F., Trumel H., Jeulin D. and Besson J. Thermoelastic properties of microcracked polycrystals. Part I: Adequacy of Fourier-based methods for cracked elastic bodies, *Int. J. Solids Struct.* **155** 2018, 248–256.

Gee R.H., Maiti A. and Fried L.E., Mesoscale modeling of irreversible volume growth in powders of anisotropic crystals., *Appl. Phys. Lett.* **90**, 2007, 254105.

Gibiansky V., L. and Torquato S., Thermal expansion of isotropic multiphase composites and polycrystals, *J. Mech. Phys. Solids* **45** (7), 1997, 1223–1252.

Grechka V. and Kachanov M., Effective elasticity of rocks with closely spaced and intersecting cracks, *Geophys.* **71** (3), 2006, D85–D91.

Hashin Z., Thermal expansion of polycrystalline aggregates: I. Exact analysis, *J. Mech. Phys. Solids* **32** (2), 1984, 149–157.

Jerauld G.R., Scriven L.E. and Davis H.T., Percolation and conduction on the 3D Voronoi and regular networks: a second case study in topological disorder, *J. Phys. C: Solid State Phys.* **17** (19), 1984, 3429.

Kachanov M., Effective elastic properties of cracked solids: critical review of some basic concepts, *Appl. Mech. Rev* **45** (8), 1992, 304–335.

King A., Johnson G., Engelberg D., Ludwig W. and Marrow J., Observations of intergranular stress corrosion cracking in a grain-mapped polycrystal, *Science* **321** (5887), 2008, 382–385.

Kolb J.R. and Rizzo H.F., Growth of 1,3,5-Triamino-2,4,6-Trinitrobenzene (TATB). I. anisotropic thermal expansion., *Propellants Expl. Pyrotech.* **4** (1), 1979, 10–16.

Luscher D.J., Buechler M.A. and Miller N., Self-consistent modeling of the influence of texture on thermal expansion in polycrystalline TATB., *Modell. Simul. Mater. Sci. Eng.* **22** (7), 2015, 075008.

Maiti A., Gee R.H., Hoffman D.M. and Fried L.E., Irreversible volume growth in polymer-bonded powder systems: Effects of crystalline anisotropy, particle size distribution, and binder strength., *J. Appl. Phys.*, 103, 2008, 053504.

Moakher M. and Norris A.N., The closest elastic tensor of arbitrary symmetry to an elasticity tensor of lower symmetry, *J. Elast.* **85** (3), 2006, 215–263.

Murnaghan F.D., Finite Deformation of Elastic Solids, 1951, John Wiley and sons; New York.

Naum R.G. and Jun C.K., Thermal expansion of polycrystalline graphite., *J. Appl. Phys.* 41, 1970, 5092–5095.

O'Connell R.J. and Budiansky B., Seismic velocities in dry and saturated cracked solids, *J. Geophys. Res.* **79** (35), 1974, 5412–5426.

Ponte Castañeda P. and Willis J.R., The effect of spatial distribution on the effective behavior of composite materials and cracked media, *J. Mech. Phys. Solids* **43** (12), 1995, 1919–1951.

Rath B.B. and Bernstein I.M., The relation between grain-boundary orientation and intergranular cracking, *Met. Trans.* **2** (10), 1971, 2845–2851.

Rizzo H.F., Humphrey J.R. and Kolb J.R., Growth of 1,3,5-Triamino-2,4,6,-Trinitrobenzene. II. Control of growth by use of high T_g polymeric binders, *Propellants Expl.* **6** (1), 1981, 27–36.

Rosen B.W. and Hashin Z., Effective thermal expansion coefficients and specific heats of composite materials, *Int. J. Eng. Sci.* **8** (2), 1970, 157–173.

Sevostianov I., Yilmaz N., Kushch V. and Levin V., Effective elastic properties of matrix composites with transversely-isotropic phases, *Int. J. Solids Struct.* **42** (2), 2005, 455–476.

Sigmund O. and Torquato S., Design of materials with extreme thermal expansion using a three-phase topology optimization method, *J. Mech. Phys. Solids* **45** (6), 1997, 1037–1067.

Stoyan D., Kendall W.S. and Mecke J. Stochastic Geometry and its Applications, second ed., 1995, John Wiley & Sons, Chichester.

Sun J., Kang B., Xue C., Liu Y., Xia Y., Liu X. and Zhang W., Crystal state of 1,3,5-triamino-2,4,6-trinitrobenzene (TATB) undergoing thermal cycling process., *J. Energetic Mater.* **28**, 2010, 189–201.

Watt J.P., Hashin-Shtrikman bounds on the effective elastic moduli of polycrystals with monoclinic symmetry, *J. Appl. Phys.* **51** (3), 1980, 1520–1524.

Willot F., Fourier-based schemes for computing the mechanical response of composites with accurate local fields, *Comptes Rendus Mec.* **343** (3), 2015, 232–245.

Willot F. and Pellegrini Y.-P., Fast Fourier transform computations and build-up of plastic deformation in 2D, elastic-perfectly plastic, pixelwise-disordered porous media, In: Jeulin D., Forest S. (Eds.), *Continuum Models and Discrete Systems CMDS 11*, 2008, École des Mines, Paris, 443–449, online at https://arxiv.org/abs/0802.2488.

Willot F., Trumel H. and Jeulin D. The thermoelastic response of cracked polycrystals with hexagonal symmetry, 2018. Submitted.

Xiao J., Huang Y., Hu Y. and Xiao H., Molecular dynamics simulation of mechanical properties of TATB/fluorine-polymer PBXs along different surfaces, *Sci. China Ser. B: Chem.* **48** (6), 2005, 504–510.